Repeat ridge jumps associated with plume-ridge interaction, melt transport, and ridge migration

Eric Mittelstaedt,[1,2] Garrett Ito,[1] and Jeroen van Hunen[3]

Received 24 February 2010; revised 22 August 2010; accepted 29 October 2010; published 20 January 2011.

[1] Repeated shifts, or jumps, of mid-ocean ridge segments toward nearby hot spots can produce large, long-term changes to the geometry and location of the tectonic plate boundaries. Ridge jumps associated with hot spot–ridge interaction are likely caused by several processes including shear on the base of the plate due to expanding plume material as well as reheating of lithosphere as magma passes through it to feed off-axis volcanism. To study how these processes influence ridge jumps, we use numerical models to simulate 2-D (in cross section) viscous flow of the mantle, viscoplastic deformation of the lithosphere, and melt migration upward from the asthenospheric melting zone, laterally along the base of the lithosphere, and vertically through the lithosphere. The locations and rates that magma penetrates and heats the lithosphere are controlled by the time-varying accumulation of melt beneath the plate and the depth-averaged lithospheric porosity. We examine the effect of four key parameters: magmatic heating rate of the lithosphere, plate spreading rate, age of the seafloor overlying the plume, and the plume-ridge migration rate. Results indicate that the minimum value of the magmatic heating rate needed to initiate a ridge jump increases with plate age and spreading rate. The time required to complete a ridge jump decreases with larger values of magmatic heating rate, younger plate age, and faster spreading rate. For cases with migrating ridges, models predict a range of behaviors including repeating ridge jumps, much like those exhibited on Earth. Repeating ridge jumps occur at moderate magmatic heating rates and are the result of changes in the hot spot magma flux in response to magma migration along the base of an evolving lithosphere. The tendency of slow spreading to promote ridge jumps could help explain the observed clustering of hot spots near the Mid-Atlantic Ridge. Model results also suggest that magmatic heating may significantly thin the lithosphere, as has been suggested at Hawaii and other hot spots.

Citation: Mittelstaedt, E., G. Ito, and J. van Hunen (2011), Repeat ridge jumps associated with plume-ridge interaction, melt transport, and ridge migration, *J. Geophys. Res.*, *116*, B01102, doi:10.1029/2010JB007504.

1. Introduction

[2] Mantle plume-ridge interaction alters the structure and composition [*Ito et al.*, 2003] as well as the overall geometry and location of mid-ocean ridges [*Canales et al.*, 2002; *Hardarson et al.*, 1997; *Jóhannesson*, 1980; *Jones*, 2003; *Müller et al.*, 2001; *Sæmundsson*, 1974; *Wilson and Hey*, 1995]. Changes in ridge location are often caused by a plume "capturing" a nearby ridge axis through ridge propagation [*Hey*, 1977; *Wilson and Hey*, 1995], which probably initiates by discrete shifts or "jumps" of the ridge axis [e.g., *Hardarson et al.*, 1997]. Numerous observations indicate that repeated ridge jumps at ridge–hot spot interactions [e.g., *Briais and Rabinowicz*, 2002; *Brozena and White*, 1990; *Hardarson et al.*, 1997; *Hey*, 1977; *Jóhannesson*, 1980; *Krishna et al.*, 1995; *Krishna and Rao*, 2000; *Mammerickx and Sandwell*, 1986; *Müller et al.*, 1993; *Nakanishi et al.*, 1999; *Small*, 1995] can play a significant role in the long-term evolution of the tectonic plates [*Müller et al.*, 1998, 2008].

[3] Ridge jumps toward hot spots have been estimated to occur over distances from ~10^1 km at Iceland [*Garcia et al.*, 2003; *Hardarson et al.*, 1997] to ≤800 km at Shatsky Rise [*Nakanishi et al.*, 1999] and often occur repeatedly along a single ridge segment as the distal sections of the overall ridge axis migrate away from the hot spot. For example, Iceland has experienced at least four ridge jumps toward the presumed plume center in the last 16 Myr [*Hardarson et al.*, 1997; *Jóhannesson*, 1980] as the Mid-Atlantic Ridge has migrated NNW relative to the hot spot [*Jones*, 2003; *Torsvik et al.*, 2001]. Repeat ridge jumps are also observed at the Galápagos [*Hey*, 1977], the Ninety-East Ridge [*Krishna et al.*, 1995; *Krishna and Rao*, 2000], and possibly the Louisville hot spot [*Small*, 1995].

[1]SOEST, University of Hawaii at Manoa, Honolulu, Hawaii, USA.
[2]Now at Laboratoire FAST, CNRS/UPMC/UPS, Orsay, France.
[3]Department of Earth Sciences, Durham University, Durham, UK.

0148-0227/11/2010JB007504

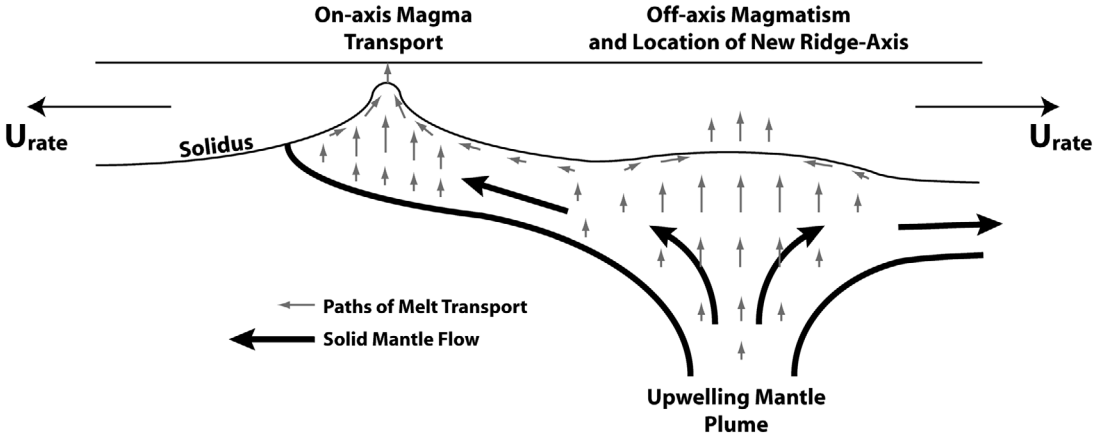

Figure 1. Conceptual model of an upwelling, near-ridge mantle plume, melting, melt transport, and magmatic heating of the lithosphere. Melting generated in the mantle is transported (gray, smaller arrows; all arrows are illustrative only) vertically and then along the solidus at the base of the lithosphere toward local minima in solidus depth where it collects until it builds sufficient pressure to penetrate the lithosphere. Shear stresses are imposed upon the lithosphere due to the solid flow of the upwelling mantle plume (black, large arrows).

[4] Two of the principal factors necessary for a ridge jump are weakening of off-axis lithosphere and a stress field that promotes rifting. One mechanism proposed to weaken the lithosphere is the thermal and mechanical erosion of the lithosphere by a laterally spreading mantle plume (i.e., plate "rejuvenation") [e.g., *Li et al.*, 2004; *Ribe and Christensen*, 1994]. Another proposed weakening mechanism is heating of the lithosphere as magma passes through it [*Mittelstaedt et al.*, 2008]. In fact, thermal as well as mechanical weakening by magma has been suggested to be important to the initiation of rifting in the Gulf of Aden [*Kendall et al.*, 2005], during the initial breakup of the North Atlantic [*Nielsen et al.*, 2002], to the creation of continental microplates [*Müller et al.*, 2001], and to play a key role in determining the location of hot spot islands [*Hieronymus and Bercovici*, 2001]. The lithospheric stresses that promote ridge jumps can be due to far-field tectonic stresses, shear tractions on the base of the lithosphere induced by a laterally spreading plume, and plate-parallel gravitational stresses due to buoyant uplift of the lithosphere.

[5] In previous work, *Mittelstaedt et al.* [2008] examined the contribution of thermal weakening of the lithosphere due to magma penetration at a near-ridge hot spot to ridge jumps. Our method involved imposing magmatic heating in a zone of fixed width and at a rate proportional to the temperature contrast between magma and the lithosphere while the lithospheric stress field was controlled by far-field tension driving plate spreading. The results suggest that magmatic heating alone can cause ridge jumps, but only on young, slow moving lithosphere. One shortcoming of these models was the inability to predict repeat ridge jumps as the ridge migrates away from the hot spot.

[6] This study builds upon our previous work by including the contribution of a plume-like upwelling and a new description of magmatic heating that includes mantle melting and melt transport. The goal is to investigate the most basic mechanical processes that control ridge jumps associated with plume-ridge interaction. While the documented natural occurrences of ridge jumps have distinct and sometimes unique characteristics, we aim to examine the factors that are likely to be important to all plume-related ridge jumps and quantify the effects of particular geologic variables. We thus quantify the behavior of ridge jumps in stationary and migrating systems, for different plume-ridge separation distances, spreading rates, plume temperatures and buoyancy fluxes, and different heating rates of the lithosphere by magma. The new models are the first to spontaneously predict repeat ridge jumps as well as other dynamical behaviors including single jumps, capture of the ridge by the hot spot, and dueling between the new and old rifts. Additionally, magmatic heating of the lithosphere predicted by our models provides another possible mechanism for thinning of the lithosphere above intraplate plumes, such as Hawaii.

2. Conceptual and Mathematical Model

2.1. Conceptual Model

[7] Figure 1 illustrates the concepts that set the frame work of our mathematical and numerical model. A hot, off-axis mantle plume rises, melts, and spreads laterally as it encounters the lithosphere. The buoyant melt percolates vertically through the mantle until it reaches the top of the melting region (i.e., the solidus) where it accumulates within a high-porosity layer just below the cooler, low-permeability lithosphere. Melt flows along the base of the lithosphere toward a locally eroded depth minimum over the plume. As melt accumulates, it builds pressure on the overlying lithosphere. When the melt pressure is high, fractures open in the lithosphere and allow magma to travel to the seafloor. As the magma passes through and heats the plate, the plate thins and weakens. If the weakening is sufficient, stresses associated with plate motion and the spreading plume initiate rifting off-axis. Eventually, spreading shifts from the old to the new ridge axis.

2.2. Mathematical and Numerical Model of Viscous Mantle Flow

[8] We use the finite element code CITCOM [*Moresi and Solomatov*, 1995; *van Hunen et al.*, 2005; *Zhong et al.*,

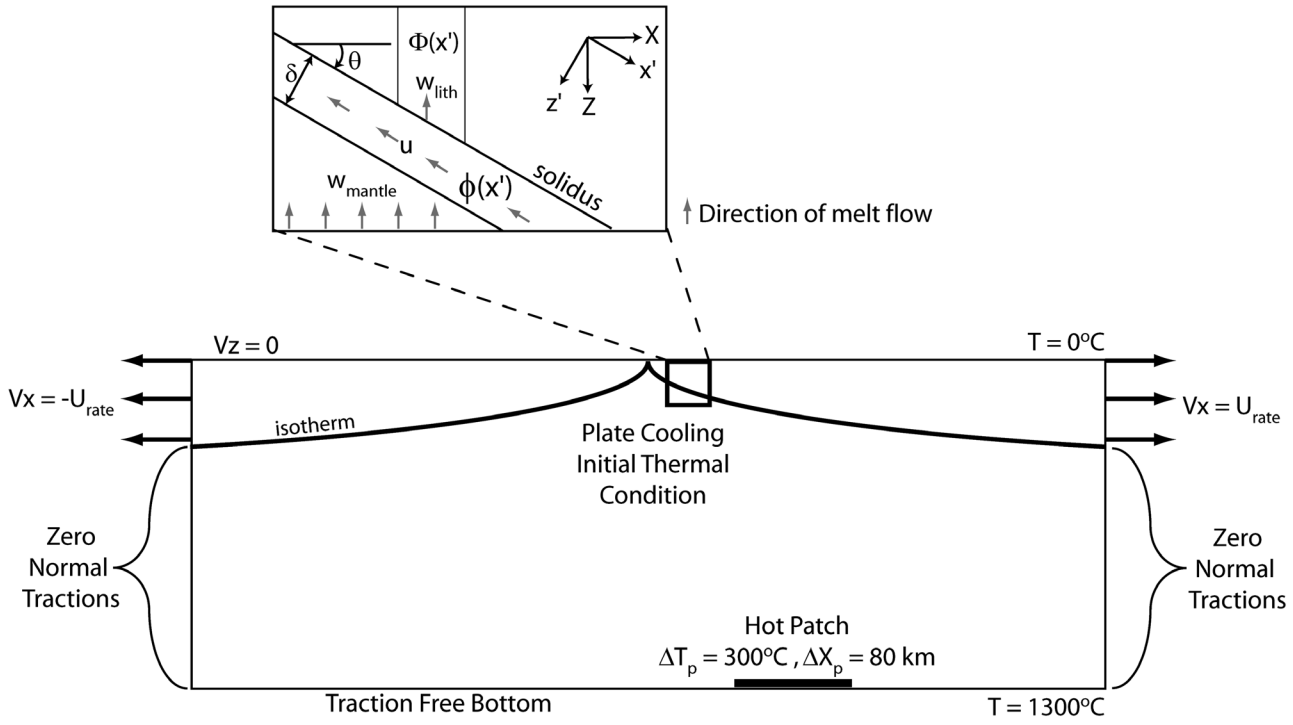

Figure 2. A cartoon of the boundary and initial conditions of the model and the geometry of melt transport. See text for a description of the boundary and initial conditions. (inset) Melt is transported vertically through the mantle (w_{mantle}) until it encounters the solidus where it accumulates and travels along the base of the lithosphere, which slopes at angle θ down from the horizontal. Melt flow rate through the lithosphere (w_{lith}) is controlled by the porosity (ϕ) beneath the solidus and the average porosity of the lithosphere (Φ).

2000] to solve the 2-D equations of conservation of energy, momentum, and mass in a viscoplastic mantle. The model domain measures 1200 km laterally and 400 km vertically and is discretized into 512 by 128 elements, respectively. The height and width of each element range between 1.5 km and 3.2 km with the highest resolutions in the upper 50 km and in the region of plume-ridge interaction. The vertical sides of the model are traction free at depths >80 km, where the hot, low-viscosity asthenosphere is present, and are imposed to move at a horizontal velocity at shallower depths, where the cooler and stiff lithosphere is present, to drive plate spreading (Figure 2). The horizontal upper surface is shear traction free with a zero vertical velocity; the bottom boundary is traction free (i.e., an open boundary). The thermal boundary conditions include insulating sides and imposed potential temperatures of 0°C and 1300°C at the top and bottom boundaries, respectively. Within the model domain, the initial temperature condition is that of the plate model [e.g., *Parsons and Sclater*, 1977] in which the lithosphere is thinnest at the ridge and increases to a maximum thickness of 125 km.

[9] To initiate a plume-like upwelling, a hot patch is imposed along the bottom of the model with a temperature anomaly defined by $\Delta T = \Delta T_p \exp(-\Delta x^2/(\Delta x_p/2)^2)$, where Δx is the horizontal distance from the plume center. The maximum plume temperature of ΔT_p = 300°C and the temperature anomaly width of Δx_p = 80 km result in a plume buoyancy flux of ~2000 kg s^{-1} (assuming a cylindrical plume stem) similar to estimates for many hot spots [*Sleep*, 1990; *van Hunen and Zhong*, 2003; *Zhong and Watts*, 2002]. See Table 1 for all model parameters.

[10] Ductile deformation in the model depends on an Arrhenius function of viscosity with temperature

$$\eta = \eta_0 \exp\left[\frac{E}{R}\left(\frac{1}{T} - \frac{1}{T_0}\right)\right], \quad (1)$$

where η_0 is the reference viscosity of 2.2×10^{19} Pa s defined at a temperature T equal to the basal temperature (T_0 = 1300°C), a value similar to that predicted by the joint modeling and seismic study of *van Hunen et al.* [2005] and R is the ideal gas constant. The activation energy E = 180 kJ mol^{-1} is less than experimental values (E = 540 kJ mol^{-1}, olivine [*Karato and Wu*, 1993], dislocation creep) to simulate the effects of a stress-dependent rheology [e.g., *Christensen*, 1984; *van Hunen et al.*, 2005]. We do not consider retained melt fraction [*Hirth and Kohlstedt*, 1995a, 1995b] or extracted water [*Hirth and Kohlstedt*, 1996] because they have competing effects on viscosity, with a net effect that is not well understood in natural settings. The above assumptions are designed to address the first-order causes of ridge jumps.

[11] To approximate faulting behavior, we simulate Coulomb-Navier plasticity [e.g., *Davis and Selvadurai*, 2002] through an additional viscosity law that depends upon the strain history as well as the stress. Plastic yielding

Table 1. Model Parameters

Parameter	Description	Value	Units	Equation First Used
A_0	Constant on melt pressure below lithosphere	-	Pa	(A15)
C_0	Dimensional constant in melt transport calculation	-	Pa	(13)
c_p	Heat capacity of the mantle at constant pressure	1250	J °C^{-1} kg^{-1}	(6)
D'	Nondimensional constant in melt transport calculation	0.625	-	(14)
E	Activation energy	180	kJ mol^{-1}	(1)
F	Melt fraction	-	-	(6)
g	Acceleration of gravity	9.81	m s^{-2}	(8)
H, H_0	Fractional time-integrated magma flow rate, reference magmatic damage	-, 1000	m	(13), (16)
k_0	Reference permeability	1×10^{-10}	m^2	(8)
L_0, L_0'	Parameter controlling the sensitivity of lithospheric porosity to accumulated damage	-, 0.005	Pa m^{-1}, -	(13), (14)
n	Exponent on porosity in the permeability	2	-	(10)
P	Pressure	-	Pa	(6)
Pe	Peclet number	0.2	-	(10)
Q_{thin}	Spreading rate times the integrated heat lost from the numerical thermal field a distance ΔX from the ridge axis at $t = 0$	-	J m^{-1} s^{-1}	(18)
Q_{cool}	Spreading rate times the integrated heat lost from a half-space cooling model a distance ΔX from the ridge axis	-	J m^{-1} s^{-1}	(19)
q	Heating rate at a point due to magma penetrating the lithosphere	-	J m^{-3} s^{-1}	(17)
R	Ideal gas constant	8.3	J K^{-1} kg^{-1}	(1)
S	Healing rate scale	3×10^{-4}	m^3 s^{-1}	(16)
ΔS	Entropy change associated with converting a solid to a liquid	200	J K^{-1} kg^{-1}	(6)
t_{age}	Age of the lithosphere where a ridge jump occurs	-	Myr	(19)
t_{jump}	Time between initiation of magmatic heating and completion of a ridge jump	-	Myr	(A21)
T, T_{asth}	Potential temperature, potential temperature of normal asthenosphere	-, 1300	°C	(1), (17)
ΔT_p	Excess plume temperature	300	°C	-
U_{rate}	Half spreading velocity	10–30	km Myr^{-1}	(15a), (15b)
u, w	Melt flow rate parallel and perpendicular to the solidus	-	m s^{-1}	(7), (7)
U, W	Horizontal and vertical velocities of the solid matrix	-	m s^{-1}	(9)
u_0	Lateral melt flow rate scale	-	m s^{-1}	(A11k)
w_{lo}, w_{mo}	Scale of lithospheric melt flow rate, scale of mantle melt flow rate	7.9×10^{-10}, 4.9×10^{-10}	m s^{-1}	(A11k), (A11f)
w_{mantle}, w_{lith}	Melt flow rate from below, melt flow rate through the lithosphere	-	-	(9), (10)
w_{lith}^{max}	Maximum melt flow rate through the lithosphere before a ridge jump	-	-	(18)
w_{l0}/w_{m0}	Ratio of melt flow rate scales	1.6	-	(12)
X, Z	Horizontal and vertical coordinates in absolute reference frame	-	m	(15a), (15b), (16)
x, z	Solidus parallel and perpendicular coordinate directions			(7)
ΔX	Distance between initial rifting and the current ridge axis	-	m	(A22)
$Z_{solidus}$, Z_{max}	Top and bottom depths of the melting region	-	m	(9)
Z_{lith}	Lithospheric thickness above the hot spot	-	m	(17)
ΔZ	Thickness of high-porosity layer	1000	m	(8)
α	Coefficient of thermal expansion	3.5×10^{-5}	J °C^{-1} kg^{-1}	(6)
β	Magmatic heating rate scale	$(0.9–10) \times 10^{-5}$	m^{-1}	(17)
γ	Coefficient of static friction	0.6	-	(3)
δ	Length scale in melt transport calculation	1000	m	(A11a)
ε_p, ε_{crit}	Accumulated plastic strain, critical strain	-	s^{-1}	(3), (5)
$\dot{\varepsilon}_1$, $\dot{\varepsilon}_3$	Maximum and minimum principal strain rates	-	s^{-1}	(4)
η, η_0	Mantle viscosity, reference mantle viscosity	$10^{18–24}$, 2.2×10^{19}	Pa s	(1)
μ_m	Melt viscosity	1	Pa s	(8)
θ	Angle of the solidus down from the horizontal	-	-	(8)
κ	Thermal diffusivity	3×10^{-6}	m^2 s^{-1}	(19)
ρ, ρ_m	Solid density, melt density	3300, 2800	kg m^{-3}	(6), (7)
$\Delta\rho$	Difference between solid and melt densities	500	kg m^{-3}	(A11i)
σ_1, σ_3	Maximum and minimum principal stresses	-	Pa	(2)
σ_p	Melt pressure beneath the solidus	-	Pa	(13)
σ_{ys}	Yield stress	-	Pa	(2)
σ_{coh}, σ_{coh}^{ref}, σ_c	Cohesion in weakening, cohesion reference value, inherent strength of lithosphere (constant)	-, 44, -	MPa	(3), (5), (13)
τ	Time scale in melt transport calculation	-	s	(A11b)
ϕ, ϕ_0	Porosity along the solidus, reference porosity	-, 0.1, 2.2	-	(7), (A11a)
Φ, Φ_{max}	Characteristic porosity of the lithosphere, maximum lithospheric porosity	-		(10), (13)

occurs when the difference between the maximum (most tensile) σ_1 and minimum (least tensile) σ_3 principal stresses is greater than the yield stress,

$$(\sigma_1 - \sigma_3) > \sigma_{ys}, \tag{2}$$

where the yield stress is defined by

$$\sigma_{ys} = \frac{1}{\sqrt{\gamma^2 + 1}} \left[2\sigma_{coh}(\varepsilon_p) \pm \gamma(\sigma_1 + \sigma_3) \right], \tag{3}$$

where γ is the coefficient of static friction and σ_{coh} is the cohesion, which is a function of ε_p, the accumulated plastic

strain, equal to the sum of strain minus a linear healing rate (characteristic healing time ~300 kyr) where (2) is true. The criteria in equation (2) is implemented numerically by iteratively adjusting the viscosity of elements where $(\sigma_1 - \sigma_3) > \sigma_{ys}$ to

$$\eta = \frac{\sigma_{ys}}{(\dot{\varepsilon}_1 - \dot{\varepsilon}_3)}, \tag{4}$$

where $\dot{\varepsilon}_1$ and $\dot{\varepsilon}_3$ are the maximum and minimum principal strain rates, respectively. This method is similar to that used by *Chen and Morgan* [1990], with the important difference that the cohesion σ_{coh} decreases with accumulated plastic strain ε_p, a dependence that leads to more localized deformation at plate boundaries. The weakening law we have adopted is

$$\sigma_{coh} = \sigma_{coh}^{ref}\left(1 - \frac{\varepsilon_p}{\varepsilon_{crit}}\right), \tag{5}$$

where α_{coh}^{ref} (= 44 MPa) is the reference cohesion prior to any strain, ε_{crit} = 0.5 [*Poliakov and Buck*, 1998]. As ε_p is a material variable, we track its advection using tracer particles [*Bianco et al.*, 2008]. This method forms regions of plate rifting across ~10–20 elements with faster spreading rates leading to more focused deformation. Thus, the model resolution of ~1.5 km in the region of plume-ridge interaction allows for plate boundary widths of 15–30 km for half spreading rates between 10 and 30 km Myr^{-1}.

2.3. Mantle Melting

[12] We use a description of decompression melting of a dry, peridotite mantle to calculate melt productivity $\partial F/\partial P$ where F is the melt fraction and P is pressure. The melting region is bounded by the peridotite solidus $T_{solidus}$ of *Katz et al.* [2003, Figure 1]. At a given pressure P, when the potential temperature T surpasses $T_{solidus}$, a constant $\partial T/\partial F$ and a constant change in entropy ΔS (associated with converting a solid to a liquid) are used to calculate $\partial F/\partial P$ [e.g., *Asimow et al.*, 2004; *Ito and Mahoney*, 2005; *Katz et al.*, 2003]

$$-\frac{\partial F}{\partial P} = \frac{\left(\frac{\partial T}{\partial P}\right)_F - \frac{\alpha T}{\rho c_p}}{\left(\frac{\partial T}{\partial F}\right)_P + \frac{T\Delta S}{c_p}}, \tag{6}$$

where α is the coefficient of thermal expansivity, c_p is the heat capacity at constant pressure, and ρ is the mantle density. The value of $\partial T/\partial F$ and ΔS are chosen (see list of symbols in Table 1) so that the model predicts a normal ridge crustal thickness of 6–7 km in the absence of a mantle plume. The value of F is limited to ~0.2 to simulate the strong reduction in $\partial F/\partial P$ when cpx is completely melted [*Asimow et al.*, 1997, 2004]. This parameterization is very simple; the only variations of $\partial F/\partial P$ with depth are associated with the slope of the solidus and not, for example, with water content or mineralogy. More realism is not needed because what is most essential to this study is the ability to simulate self-consistent changes in melt flux reaching the solidus at the base of the lithosphere in response to local fluctuations in mantle temperature and flow.

2.4. Melt Transport and Penetration of the Lithosphere

[13] The melt transport equations used here are based on those introduced by *McKenzie* [1984] to describe the conservation of mass and momentum of a two-phase system (see Appendix A). We assume that the shear and effective bulk viscosities of the matrix are too low for pressure gradients associated with solid shear or compaction to influence melt flow. At the top of the melting region (i.e., the solidus), where $T \le T_{solidus}$, freezing melt makes a boundary that is impermeable to flow and leads to formation of a high-porosity channel [*Sparks and Parmentier*, 1991, 1994; *Spiegelman*, 1993]. As a result of the above assumptions, pressure gradients associated with melt buoyancy alone cause melt to rise vertically in the melting zone and to flow laterally along the sloping solidus near the base of the lithosphere.

[14] It is the lateral transport of melt along the base of the lithosphere and vertical penetration of melt through the lithosphere that is essential to the model results. Here, lateral melt flow is controlled by the average porosity (volume fraction of melt) ϕ in the high-porosity channel below the freezing boundary, whereas melt flux across the freezing boundary (through the lithosphere) is controlled by the depth-averaged porosity of the lithosphere Φ. The time-dependent melt transport along and across the solidus is described by (Appendix A)

$$\frac{\partial \rho_m \phi}{\partial t} + \rho_m\left(\frac{\partial u}{\partial x} + \frac{\partial w}{\partial z}\right) = 0, \tag{7}$$

$$u = \frac{-k_0\phi^n}{\mu_m}(\rho_s - \rho_m)g\left[\sin(\theta) + \Delta Z\frac{\partial \phi}{\partial x}\right], \tag{8}$$

$$w_{mantle} = -\int_{Z_{\max}}^{Z_{solidus}}\left(\frac{dF}{dP}\right)\rho_s g W dZ, \tag{9}$$

$$w_{lith} = \frac{-k_0\Phi^n}{\mu_m}(\rho_s - \rho_m)g\cos(\theta), \tag{10}$$

where u is the Darcy melt flow rate times porosity parallel to the solidus; w is the melt flow rate perpendicular to the solidus; W is the vertical velocity of the matrix (capital letters indicate solid velocities); ρ_m is the melt density and ρ_s is the solid density; n = 2 is the exponent relating porosity to permeability. See Table 1 for the definition of other variables. Equation (7) describes conservation of melt mass whereas equation (8) describes Darcy flow (conservation of momentum) of the melt in the direction parallel to the solidus x. The assumption of 1-D melt transport along the solidus allows us to solve separately the equations defining melt supply created in the mantle below the high-porosity channel, w_{mantle} (9), and that penetrating the lithosphere above the channel, w_{lith} (10, discussed below), the difference of which is used to compute $\partial w/\partial z$ in equation (7).

[15] To isolate the fundamental parameters that govern porosity in the channel, we combine (7) and (8), make variables dimensionless (denoted by primes) as described in

Appendix A, and derive the dimensionless governing equation (see Table 1 for definition of all variables),

$$\frac{\partial \phi'}{\partial t'} - \frac{\partial}{\partial x'}\left[\phi'^{n}\frac{\partial \phi'}{\partial x'}\right] - Pe\left[\phi'^{n-1}\sin(\theta)\frac{\partial \phi'}{\partial x'} - \frac{\phi'^{n}}{n}\cos(\theta)\frac{\partial \theta}{\partial x'}\right] = w'_{mantle} - \frac{w_{l0}}{w_{m0}}w'_{lith}. \quad (11)$$

Two input parameters control melt transport: the Peclét number Pe, and the ratio of scales for the flow rate of melt through the lithosphere and up from the mantle w_{l0}/w_{m0}.

[16] The other essential aspect of the magma transport model is to simulate when and where magma actually penetrates the lithosphere (i.e., where and when $w'_{lith} > 0$). Equation (10) describes the depth-averaged magma flux (per area) through the lithosphere w_{lith} due to general mechanisms which could include intergranular porous flow, interconnected melt channels, and diking. As such, w_{lith} depends on the average fraction of melt in the lithosphere, or porosity Φ. Following a methodology similar to that of *Hieronymus and Bercovici* [2001], we assume that changes in Φ are caused by changes in the excess pressure of the magma just below the plate σ_p and lithospheric damage (generally to include chemical, thermal, and structural damage) caused by magma passing through the plate (see Appendix A)

$$\Phi = \frac{\Phi_{\max}}{2}\left[1 + \tanh\left(\frac{\sigma_p - \sigma_c + L_0 H}{2C_0/\Phi_{\max}}\right)\right], \quad (12)$$

where L_o and C_o are constants, σ_c is the inherent (constant) strength of the lithosphere, $\Phi_{\max}$ is the maximum permitted lithospheric porosity, and H is a fraction of the integrated melt flux, a measure of the accumulated magmatic damage (described below).

[17] We normalize σ_p and σ_c by a pressure scale that is proportional to ϕ_0, and normalize H by H_0 to derive the nondimensional form of (10)

$$w'_{lith} = \cos\theta\left[1 + \tanh\left(\frac{\phi'\cos\theta}{D'} - \frac{\sigma'_c}{D'} + \frac{L'_0 H'}{D'}\right)\right]^{n} \quad (13)$$

(see Appendix for more details). Equation (13) describes the vertical melt flux across the solidus as a balance between the scaled porosity along the solidus ϕ', which controls the melt pressure from the high-porosity channel below the solidus, the scaled strength of the lithosphere σ'_c, the sensitivity to magmatic damage L'_0, where $L'_0 H'$ is a measure of the accumulated lithospheric damage due to prior magmatism, and the scale factor D'. The total damage is not permitted to exceed the strength of the lithosphere (i.e., $L'_0 H' \le \sigma'_c$). In practice, this limit is rarely reached for the chosen value of L'_0 (Table 1). Three free parameters control equation (13): σ'_c, L'_0, and D'.

[18] Lithospheric damage is assumed to occur through thermal, chemical, or physical mechanisms of recent volcanism. The quantity that measures this damage is H and is calculated using the following (dimensional) advection equation

$$\frac{\partial H}{\partial t} = w_{lith} - \frac{\partial (H U_{rate})}{\partial X} - \frac{S}{(H + H_0)^2}, \quad (14)$$

where X is the lateral coordinate in the absolute reference frame (i.e., not along the solidus). With only the first term on the right-hand side, H would equal $\int w_{lith} dt$, the time-integrated magma flow through a given section of lithosphere. The second term on the right hand side describes advection of damage with a plate migrating horizontally at a half spreading rate of U_{rate}, and the third term describes the reduction of damage by healing. With this formulation (see Appendix for details), more damaged lithosphere (larger H) heals more slowly than less damaged lithosphere (smaller H; an analogous behavior is seen in concrete compression experiments [*Zhong and Yao*, 2008]), and the damage initiated in pristine lithosphere heals at a maximum rate of S/H_0^2. This maximum healing rate sets the minimum magma penetration rate w_{lith} where damage begins to accumulate. Equation (14) introduces one more free parameter, S.

[19] In summary, (11), (13), and (14) control magma flow in the asthenosphere and through the lithosphere. The following procedure is used to solve these equations and couple them to the calculations of mantle melting and temperature each time step. First, the location and slope of the solidus are determined from the solutions of solid flow and heat transfer. Next, the melt supply from below w_{mantle} is calculated from (9). The value of w_{lith} at each point along the solidus is found using (13) with the damage variable H from the previous time step. Equation (11) is then solved for the transport of melt along the solidus. Finally, H is updated using equation (14). Analytical solutions of (11) are used to verify the method (Appendix A). The free parameters are Pe, w_{l0}/w_{m0}, H_0, L'_0, D', and S (see Table 1 for values). Magmatic heating of the lithosphere is calculated as described in section 2.5.

2.5. Magmatic Heating

[20] In a formulation similar to that of *Mittelstaedt et al.* [2008], the (dimensional) magmatic heating rate at each point in the lithosphere is defined as

$$q = \rho c_p \beta w_{lith}[T_{asth} - T(X, Z, t)] \quad (15a)$$

$$q_{\max} \equiv \rho c_p T_{asth} \beta w_{lith}^{\max}, \quad (15b)$$

where T_{asth} is the temperature of both the nonplume asthenosphere and the penetrating magma (1300°C), β (m^{-1}) is a constant scale factor controlling the heating rate, w_{lith} ($m\ s^{-1}$) is the magma penetration rate (or volumetric flux per unit cross-sectional area) through the lithosphere which reaches a maximum value $w_{lith}^{\max}$ before a ridge jump, X and Z are coordinates of the absolute reference frame, and $q_{\max}$ is the maximum heating rate before a ridge jump (used in our scaling analysis, section 3.3). Consistent with (13), which describes melt flux through the lithosphere, (15a) is designed to be as general as possible and to not require a specific melt transport mechanism in the lithosphere (see *Mittelstaedt et al.* [2008] for further discussion).

[21] We examine cases with w_{lith} calculated from (11)–(14) and a constant value of β (β is varied between 9×10^{-6} m^{-1} and 10×10^{-5} m^{-1}) in (15a). To explore a range of model behaviors, cases are run with half spreading rates of 10, 20, and 30 km Myr^{-1}, plate ages above the center of plume upwelling between 3 and 15 Myr, and for a few cases, we vary

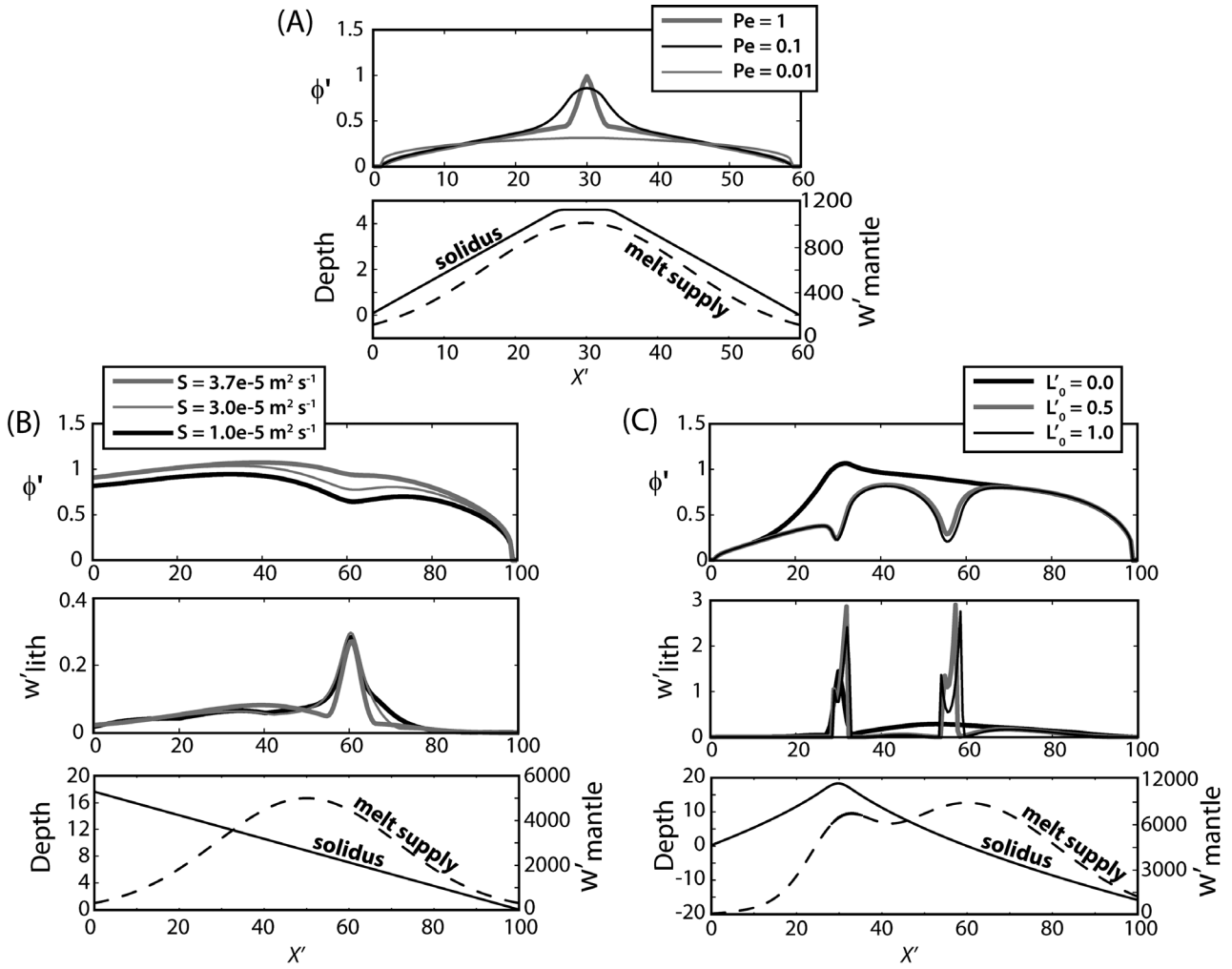

Figure 3. The three principle free parameters in the melt transport calculation, (a) *Pe*, (b) *S*, and (c) L'_0, along with the shape of the solidus (labeled solid line) and the mantle melt supply (w'_{mantle}; labeled dashed line) control the scaled melt flow rate through the lithosphere (w'_{lith}) and the porosity (ϕ') just beneath the solidus. See the text for a description of each case.

excess plume temperature and buoyancy flux. Additionally, we consider some cases where the plume and ridge migrate relative to each other.

3. Results

3.1. Controlling Parameters of Melt Transport: Simplified Test Cases

[22] Six free parameters control melt transport along and through the lithosphere. Various tests reveal that final model predictions are relatively insensitive to w_{l0}/w_{m0}, H_0, and D' and most sensitive to the three parameters *Pe*, L'_0, and *S*. The effects of *Pe*, L'_0, and *S* are explored with a set of preliminary calculations that involve solving (11)–(14) alone, without the Citcom calculations of mantle flow and temperature (Figure 3).

[23] First, we examine how flow along the solidus is influenced by *Pe*, which governs the relative importance of solidus slope versus lateral variations in ϕ'. The problem examines the steady state porosity beneath a solidus that is shallowest at $X' = 30$ and slopes away from this point, much like that beneath a lithospheric plate as it thickens away from a ridge axis (Figure 3a) (X is the horizontal dimension and $X' = X/\delta$ is dimensionless). In this test case, the melt supply from below is a Gaussian function of X' also centered at $X' = 30$, $L'_0 = 0$ (melt escapes out of the ridge center at $X' = 30$, but no damage accumulates), $S = 8 \times 10^{-5}$ m^2 s^{-1}, and $\phi' = 0$ is the boundary condition on the left and right sides of the domain. Smaller values of *Pe* tend to reduce lateral porosity variations, whereas larger values of *Pe* lead to a local peak in porosity (melt accumulation) where the solidus is shallowest (Figure 3a).

[24] The second test case (Figure 3b) demonstrates the effect of the healing rate scale *S* on the focusing of magma penetration through the off-axis lithosphere. Roughly simulating a ridge and an off-axis hot spot, the solidus slopes at a constant angle (10°) down to the right away from the hypothetical ridge axis (at $X' = 0$) and the melt supply from below is highest at $X' = 50$ (Figure 3b). Accumulated lithospheric damage (proportional to) H' is advected to the right at a constant velocity (10 km Myr^{-1}) with the plate, $\phi' = 0$ on the right edge, and $\partial\phi'/\partial X' = 0$ at the left edge. With *Pe* =

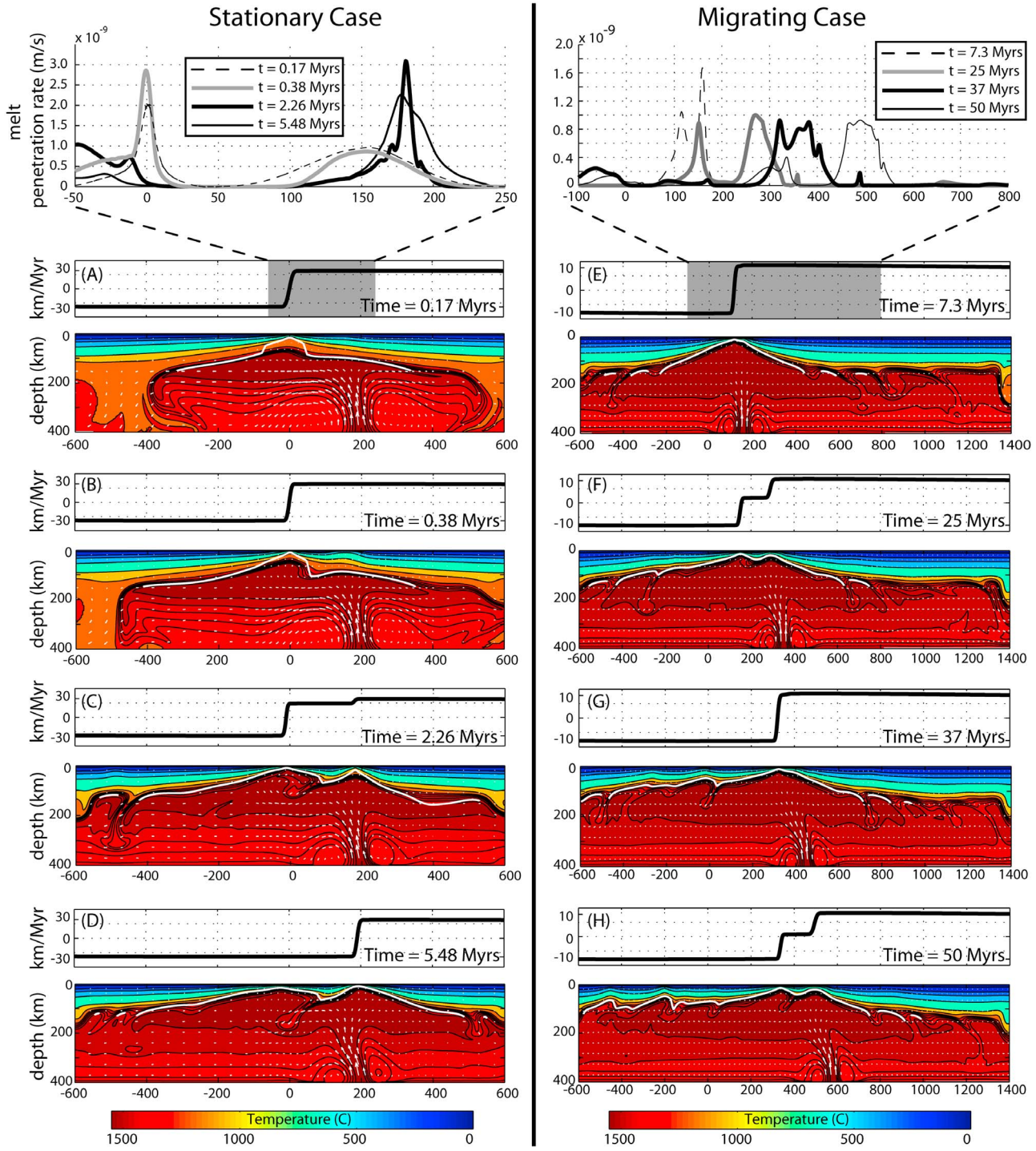

Figure 4. The temporal evolution of two cases with a (left) fixed plume location (X = 200 km) and (right) with a migrating plume. Colors show contours of potential temperature (see scales at bottom) with arrows representing mantle flow and a white contour marking the solidus at the top of the melting zone. Horizontal velocities across the top of the model (thick black lines) are shown above each set of temperature contours. Figures 4a and 4b at top show the magma flux crossing the solidus into the lithosphere in the region of interest for each case (line colors/styles correspond to the times marked for each panel).

0.022 and L_0' = 0.17, a local peak in magma penetration rate occurs just to the right of the peak in (hot spot) magma flux (cases are shown at dimensional time t = 1 Myr). Larger values of S lead to more focused zones of damage because they restrict the distance over which magma penetration is large enough to initiate damage (equations (13) and (14)) (Figure 3b).

[25] Finally, the third case discussed here demonstrates how the sensitivity (L_0') of w'_{lith} to damage affects the width and location of magma penetration through the lithosphere

(equation (13)). Resembling a situation of hot spot–ridge interaction, the solidus deepens with the square of the distance from a "ridge axis" which is centered at $X' = 30$; the melt supply from below is equal to the sum of two Gaussians with peaks at $X' = 30$ and at $X' = 60$ (the "ridge" and "plume" melt supplies), and $\phi' = 0$ imposed on the left and right edges (Figure 3c); $Pe = 0.1$, and $S = 6.5 \times 10^{-6}$ m^2 s^{-1}. Once damage begins to accumulate, larger values of L_0' lead to greater fluxes of magma penetrating the lithosphere. The greater magma fluxes cause more damage to accumulate and reduce the healing rate, which together cause a positive feedback that focuses the magma penetration at two narrow peaks (Figure 3c), one at the ridge axis and one over the hot spot.

[26] The restriction of magma penetration to such narrow zones (e.g., comparable to the width of a hot spot island) is essential for the associated magmatic heating to sufficiently weaken the lithosphere for a ridge jump. The final chosen values of Pe, L_0', and S (see Table 1) used in our full numerical calculations lead to eruptive zones at the hot spot and ridge across ~10–20 km for most cases, and are kept the same for all model cases below.

3.2. Time Evolution: Full Simulations With Fixed Plume-Ridge Separation Distance

[27] With the above parameters controlling melt transport fixed, full simulations of time-dependent plume-ridge interaction and melt transport are used to study the effects of the more geologically relevant parameters: β, spreading rate U_{rate}, initial lithospheric thickness Z_{lith} (or seafloor age t_{age}) at the hot spot, and relative motion between the ridge and hot spot U_{mig}. The range of values considered in these geologic parameters is relevant to a variety of natural examples, which we discuss below.

[28] The first set of calculations involve a ridge that is fixed relative to a plume (Figures 4a–4d, $U_{mig} = 0$). Melt transport and lithospheric heating are initiated after the plume impacts the lithosphere and begins to spread across the box, which defines time $t = 0$. Again, the imposed plume anomaly at the bottom of the model has a Gaussian width of 80 km and a peak excess temperature of 300°C. For the example case shown in Figure 4, the half spreading rate, U_{rate}, is 30 km Myr^{-1} and the heating parameter $\beta = 3.0 \times 10^{-5}$ m^{-1} (equation (15a)). Melting occurs beneath the ridge axis and within the plume stem. Initially ($t = 0.17$ Myr), the magma penetrating the ridge axis lithosphere comes from both the plume and ridge melting zones (generating a melt thickness of ~30–40 km) and is focused to a zone ~15 km wide; but off axis, above the plume, a small magma flux passes through the undamaged lithosphere over a broad region (~150 km wide) (Figure 4a, top). After several

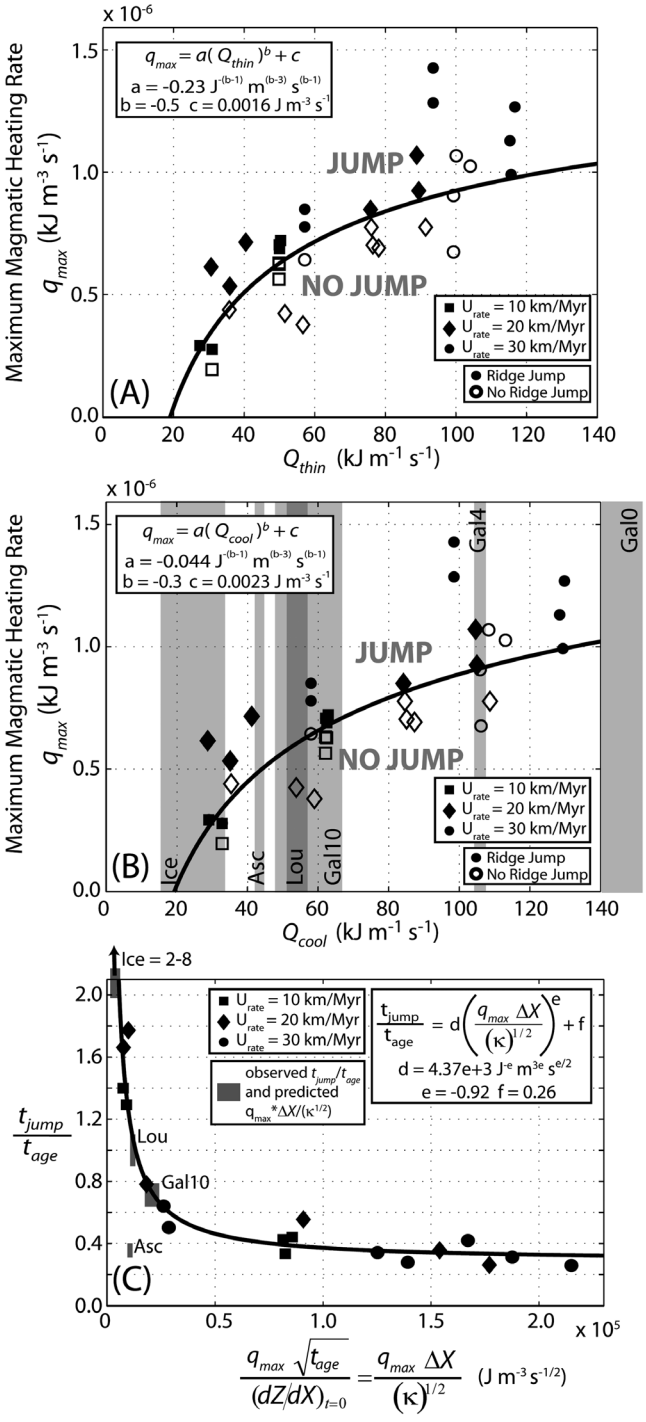

Figure 5. (a) Ridge jumps (solid symbols) occur when the value of the maximum heating rate q_{max} is above a critical value (black line) but not, in general, for values less than this (open symbols). Symbols for different spreading rates are as labeled. (b) The model results show a similar fit to the scaling law when plotted versus Q_{cool} (equations (20a) and (20b)). This relationship is used to calculate the curves in Figure 8 and to predict the minimum value of q_{max} for hot spots in Figures 5c and 6a (except for Gal0, where no jump has occurred and we predict the maximum q_{max}). Values of Q_{cool} from natural ridge–hot spot systems are denoted by vertical, transparent gray boxes. (c) The time to jump t_{jump} scaled by the age of the seafloor t_{age} to which the ridge jumps is a function of the maximum heating rate q_{max}, the thickness of the lithosphere ($Z_{lith} \sim t_{age}^{1/2}$), and the slope of the lithosphere at time $t = 0$ ($dZ_{lith}/dX \approx \partial/\partial X(\sqrt{\kappa t_{age}})$. Predicted ratios of t_{jump}/t_{age} (gray boxes) are calculated for natural plume-ridge systems (see text for details). Labels are as follows: Asc, Ascension; Gal10, Gal4, Gal0, Galapagos at 10, 4, and 0 Ma, respectively; Ice, Iceland; Lou, Louisville.

Table 2. Observations used in Figures 5 and 6

Hot Spot	U_{rate} (km Myr^{-1})	U_{mig} (km Myr^{-1})	ΔX (km)	t_{jump} (Myr)	Inferred $q_{\max}$ (kJ m^{-3} s^{-1})
Ascension	16.2–19.8	2.2–2.6	35	0.7	$0.5–0.53 \times 10^{-6}$
Galapagos, 0 Ma	27–33	25.2–30.8	260	-	-
Galapagos, 4 Ma	25–27	25.2–30.8	150[a]	-	-
Galapagos, 10 Ma	18–22	25.2–30.8	40–77[b]	1.6–2.5	$0.55–0.73 \times 10^{-6}$
Iceland	9–11	4.5–5.5	10–40	8	$0–0.38 \times 10^{-6}$
Louisville	30–36	−52	33[3]	1[c]	$0.62–0.66 \times 10^{-6}$

[a]Current plume-ridge separation distance minus 4 Myr times the ridge migration rate.
[b]The parameter t_{jump} multiplied by the ridge migration rate.
[c]The estimated width/age of magnetic anomaly 2A.

hundred thousand years, the broad off-axis magma penetration zone focuses to a narrower region (~90 km) in response to accumulating damage and local flattening of the solidus as the lithosphere thins by the plume and magmatic heating (Figure 4b). A feedback develops in which an increasing off-axis magma flux thins the off-axis lithosphere which causes the solidus to shoal near the hot spot, which further enhances magma penetration. The continued damage accumulation and thinning of the lithosphere eventually constricts the off-axis magmatism to a width comparable to that at the ridge axis. As the off-axis magma flux increases, the flux at the ridge decreases. Soon thereafter (t = 2.3 Myr) rifting over the hot spot begins, and as it does so, warm mantle material rises into the protorift which further weakens the lithosphere and promotes faster rifting. During this transfer of spreading from the old to the new ridge axis (t = 2.0–2.9 Myr), the lithosphere between the rifts acts as a microplate with very little, to no visible velocity gradients across its surface (Figure 4c). Finally, all spreading is accommodated at the new ridge axis and the old ridge is abandoned (t = 5.5 Myr, Figure 4d).

3.3. Scaling Analysis of Model Results: Fixed Plume-Ridge Separation Distance

[29] The main model results are described in terms of basic quantities that reveal the important physical processes and are themselves functions of the pertinent geologic variables. The first quantity characterizes the rate that magma heats the lithosphere. For this quantity we use $q_{\max}$ (equation (15b)), which again is the product of the heating rate factor β and the maximum magma flow rate through the off-axis lithosphere $w_{lith}^{\max}$ (1.5–3.0 × 10^{-9} m s^{-1}, which would generate ~5–40 km of excess crust if erupted at the ridge axis, spreading at U_{rate} = 10–50 km Myr^{-1}, and magmatic accretion zone 5 km wide). This quantity is analogous to the scale factor $Q_{hot\ spot}$ (total heating rate at t = 0) used by *Mittelstaedt et al.* [2008].

[30] The second quantity is a measure of the thermal resilience of the lithosphere. *Mittelstaedt et al.* [2008] defined thermal resilience as the heating rate required to thermally remove the lithosphere,

$$Q_{thin}(\Delta X) \equiv \rho c_p U_{rate}\left[\int_0^{Z_{lith}} (T_{asth} - T(\Delta X, Z))_{t=0} dZ\right], \quad (16)$$

where Z_{lith} is the initial thickness of the lithosphere a distance ΔX from the ridge axis where a ridge jump occurs or, in cases without a jump, above the plume center. Similar to *Mittelstaedt et al.* [2008], we find that for a given value of thermal resilience Q_{thin} there is a minimum value of magmatic heating rate $q_{\max}$ required to initiate a ridge jump and this value increases nonlinearly with Q_{thin} (Figure 5a),

$$q_{\max} \geq a(Q_{thin})^b + c, \quad (17)$$

where least squares regression yields $a = -0.23$ J$^{(b-1)}$ m$^{(b-3)}$ s$^{(b-1)}$, $b = -0.5$, and $c = 0.0016$ J m^{-3} s^{-1}. The lithospheric thermal resilience parameter Q_{thin}, however, does not have a straightforward relationship with commonly observed values such as seafloor age. A revised measure of the lithosphere's thermal resilience is therefore the spreading rate times the time-integrated surface heat loss of a cooling half-space:

$$Q_{cool} \equiv \int_0^{t_{age}} \frac{U_{rate}\rho c_p (T_{asth})\sqrt{\kappa\pi}}{\sqrt{t}} dt = \frac{2U_{rate}\rho c_p T_{asth}}{\sqrt{\pi}}\sqrt{\kappa t_{age}}, \quad (18)$$

in which t_{age} is the age of the seafloor at ΔX. Intuitively, through its dependence on $\sqrt{t_{age}}$, Q_{cool} is proportional to the thickness of the lithosphere predicted by a cooling semi-infinite half-space $Z_{lith} = 2\sqrt{\kappa t_{age}}$. Indeed, the minimum magmatic heating rate $q_{\max}$ needed to cause a ridge jump increases with this measure of thermal resilience much like with Q_{thin},

$$q_{\max} \geq a(Q_{cool})^b + c, \quad (19)$$

with $a = -0.044$ J$^{(b-1)}$ m$^{(b-3)}$ s$^{(b-1)}$, $b = -0.3$, and c = 0.0023 J m^{-3} s^{-1} (Figure 5b). For several natural systems with ridge jumps, we use (19) with observations of U_{rate} and t_{age} (equation (18)), to infer a minimum $q_{\max}$ for each of these systems (see Figure 5b and Table 2).

[31] Another model output quantity that closely relates to geologic observations is the predicted times from the start of magmatic heating to when the jump is complete, t_{jump}. Values are well fit if t_{jump} is normalized by seafloor age at the location of the incipient rift t_{age} (Figure 5c):

$$\frac{t_{jump}}{t_{age}} = d\left(\frac{q_{\max}\Delta X}{(\kappa)^{1/2}}\right)^e + f, \quad (20a)$$

where ΔX (= $t_{age}U_{rate}$) is the distance between the incipient rift and the initial ridge axis, $d = 4.37 \times 10^3$ J^e m^{3e} s$^{e/2}$, e = −0.92, and f = 0.26. For several natural systems, observed values of t_{jump}/t_{age} and ΔX and the minimum $q_{\max}$ inferred for these systems from equation (19) are shown for com-

parison (Figure 5c and Table 2). A relation identical to (20a) can be expressed as

$$\frac{t_{jump}}{t_{age}} = d\left(\frac{q_{\max}\sqrt{t_{age}}}{\partial Z_{lith}/\partial X}\right)^{e} + f, \qquad (20b)$$

where again $Z_{lith} = 2\sqrt{\kappa t_{age}} = 2\sqrt{\kappa \Delta X / U_{rate}}$ and $\partial Z_{lith}/\partial X$ is the slope along the base of the lithosphere at ΔX. Equations (20a) and (20b), therefore, reveal the intuitive results that ridge jumps tend to take longer to occur on older seafloor (i.e., $t_{jump} \propto t_{age}^{0.54}$), for less vigorous hot spot magmatism ($t_{jump} \propto q_{\max}^{-0.92}$), and over greater lithosphere slopes ($t_{jump} \propto (\partial Z_{lith}/\partial X)^{0.92}$). The last relation reveals that a larger solidus slope tends to channel more magma to the initial ridge axis at the expense of magma penetrating the off-axis lithosphere. These results indicate that melt transport is an important mechanism for controlling the timing of ridge jumps.

3.4. Migrating Ridges

[32] The next set of calculations simulates relative motion between the plume and ridge by moving the location of the imposed plume temperature anomaly relative to the model boundaries at a constant rate U_{mig}. The model domain for these cases is 2000 km wide with a uniform element width of ~2 km (1024 elements). Other model conditions are unchanged. The plume is initially held stationary beneath the ridge axis and is allowed to rise and spread laterally beneath the lithosphere until the thermal profile beneath the ridge is at steady state (i.e., the subridge mantle is displaced by plume material; a few million years). At this time ($t \equiv 0$) melt transport, magmatic heating, and plume migration are activated.

[33] Figures 4e–4h display an example of the time evolution for a case with a relative velocity between the plume and the original ridge axis location (U_{rate} = 10 km Myr^{-1}, U_{mig} = 10 km Myr^{-1}, $\beta = 3.0 \times 10^{-5}$ m^{-1}). Initially, all of the melt produced travels to the ridge axis, and there is negligible off-axis magmatism and heating. After the plume migrates a distance of ~50–70 km (t = 7.3 Myr), an off-axis region of melt penetration develops ~30–50 km from the ridge (Figure 4e). As the plume continues to migrate relative to the ridge, the off-axis magma flux focuses to a narrow region, the overlying lithosphere thins, and rifting pulls up warm asthenosphere, which further weakens the lithosphere until a new ridge axis forms. The time between t = 0 and the ridge jump is significantly longer (t_{jump} ~ 27 Myr) than for nonmigrating cases with the same values of the other parameters (Figure 4f). After the initial ridge jump is complete, the majority of melt from the plume travels toward the new ridge due to the steeply sloping lithosphere currently above the plume. The peak in magma flux penetrating the off-axis lithosphere is just plume-ward of the new ridge

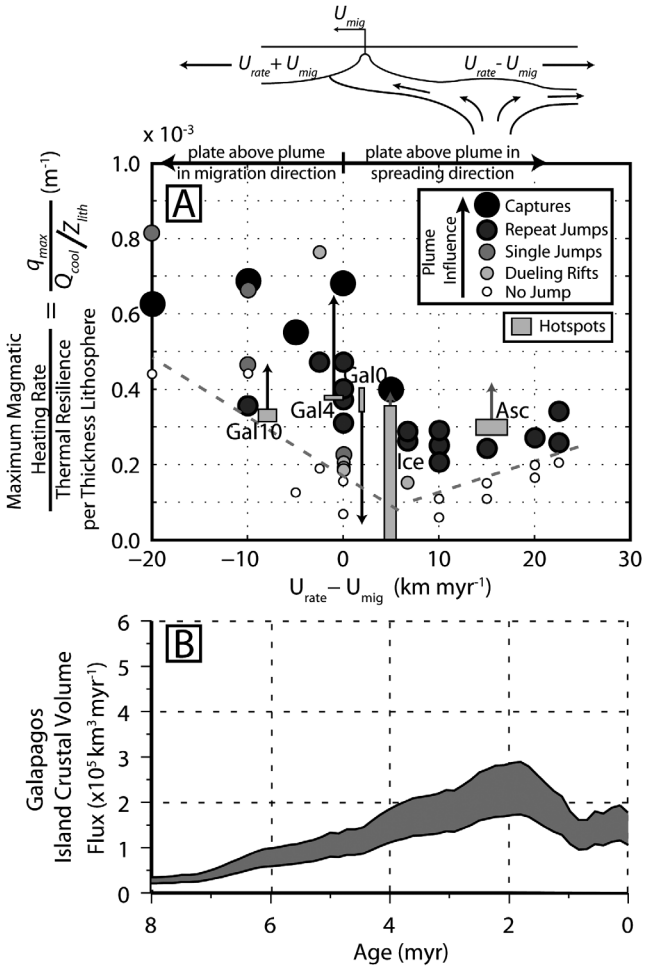

Figure 6. (a) Cases where the plume migrates relative to the ridge axis display a variety of behaviors listed in order of increasing plume influence (increasing symbol size): no jumps (white circles), two "dueling" rifts with divergence shifting between them (light gray circles), a single ridge jump (gray circles), repeat ridge jumps (dark gray circles), and immediate ridge capture (black circles). The ratio of the maximum magmatic heating rate to the lithospheric thermal resilience per thickness of lithosphere $q_{\max}/(Q_{cool}/Z_{lith})$ and the difference between the half spreading rate and the migration rate $U_{rate} - U_{mig}$ effectively describe the range of behaviors. Results suggest a maximum in plume influence for small, positive values of $U_{rate} - U_{mig}$ (gray, dashed lines). Values for natural hot spot–ridge systems (gray boxes) are placed along the horizontal axis in accordance with published spreading and ridge migration rates and along the vertical axis according minimum predicted $q_{\max}$ values required to jump in Figure 5b. Labels and references are as follows: Asc, Ascension [*Brozena and White*, 1990]; Gal0, Gal4, Gal10, Galapagos in its current configuration (0 Ma), at 4 Ma, and at 10 Ma, respectively [*Harpp and Geist*, 2002; *Wilson and Hey*, 1995]; Ice, Iceland [*Jones*, 2003; *LaFemina et al.*, 2005; *Torsvik et al.*, 2001]. See Table 2 for values used. Where ridge jumps have been observed, the predicted $q_{\max}/(Q_{cool}/Z_{lith})$ is expected to be minimal (up arrows). For the modern day Galapagos (Gal0) without jumps, the predicted $q_{\max}/(Q_{cool}/Z_{lith})$ is expected to be maximal (down arrow). At the Galapagos hot spot, $q_{\max}/(Q_{cool}/Z_{lith})$ is predicted to increase during 10–5 Ma (repeat ridge jumps to ridge capture) and to decrease during ~2.5–0 Ma (ridge capture to no jumps). (b) This predicted evolution in $q_{\max}/(Q_{cool}/Z_{lith})$ roughly mirrors the evolution of the magma volume flux at the Galapagos Islands (modified from *Ito et al.* [1997]).

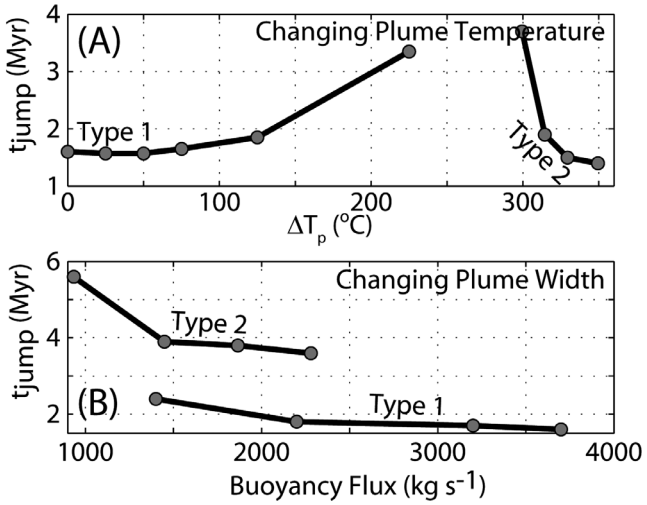

Figure 7. (a) Increasing plume temperature ΔT_p for a case of type 1 (imposed, constant magma penetration rate through the lithosphere) decreases the ridge axis strength and results in larger values of t_{jump}. Increases in ΔT_p in type 2 (melting controls magma penetration rate) cases result in sharp decreases in t_{jump} due to increasing melt supply from the mantle at the hot spot. (b) Increases in the buoyancy flux B at constant ΔT_p (changes to plume conduit width) of both type 1 and type 2 cause a decrease in t_{jump}.

axis (Figure 4g). This offset tends to make the ridge migrate with the plume, but at a slightly slower rate than the plume itself. The plume essentially "captures" the ridge for a short time. After the plume moves sufficiently far from the ridge, a new, separate peak in off-axis magma flux appears. The feedback between off-axis lithospheric thinning and enhanced melt transport begins anew until the ridge jumps a second time (t = 50 Myr) (Figure 4h).

[34] In addition to repeat ridge jumps, different values of U_{rate}, U_{mig}, and the magmatic heating rate $q_{\max}$ lead to other behaviors. Characterizing different levels of plume influence on the ridge, from least to greatest, the behaviors include no jumps (i.e., minimum influence), "dueling" rifts where each rift accommodates a fraction of the total spreading rate that varies through time, single jumps, and a rapid jump followed by continued migration of the ridge axis with the plume, i.e., complete "ridge capture" (maximum influence). The different behaviors appear to depend primarily on two quantities: $U_{rate} - U_{mig}$, the difference between the plume spreading rate and the migration rate, and $q_{\max}/(Q_{cool}/Z_{lith})$, a ratio of the magmatic heating rate to the thermal resilience per thickness of the lithosphere Z_{lith} (Figure 6). $U_{rate} - U_{mig}$, is the rate of absolute plate motion over the plume as the ridge migrates away from the plume. Note that $q_{\max}/(Q_{cool}/Z_{lith}) = q_{\max}\sqrt{\pi}/U_{rate}\rho c_p T_{asth}$ is independent of Z_{lith} because of the proportionality of Q_{cool} with Z_{lith}. Large values of $q_{\max}/(Q_{cool}/Z_{lith})$, at a given relative plate motion ($U_{rate} - U_{mig}$), lead to cases with complete ridge capture while small values of $q_{\max}/(Q_{cool}/Z_{lith})$ lead to cases without ridge jumps (Figure 6a). For $U_{rate} - U_{mig} \approx 0$ (i.e., little motion between plume and overlying plate), an increasing $q_{\max}/(Q_{cool}/Z_{lith})$ leads to a steady increase in plume influence, again from least to most: no jumps ($q_{\max}/(Q_{cool}/Z_{lith})$ ~0.1×10^{-3}), "dueling" rifts, single jumps, repeat jumps, and ridge capture ($q_{\max}/(Q_{cool}/Z_{lith})$ ~0.7×10^{-3}). The plume influence appears to be greatest (i.e., jumps begin at the lowest $q_{\max}/(Q_{cool}/Z_{lith})$) between $U_{rate} - U_{mig}$ = 0–10 km Myr^{-1} (gray, dashed lines in Figure 6a) and generally requires greater $q_{\max}/(Q_{cool}/Z_{lith})$ for the same behavior as $U_{rate} - U_{mig}$ deviates away from the point of maximum influence near 0–10 km Myr^{-1}. At a fixed $q_{\max}/(Q_{cool}/Z_{lith})$, for example $q_{\max}/(Q_{cool}/Z_{lith}) \approx 0.2 \times 10^{-3}$ m^{-1}, cases with $U_{rate} - U_{mig} \approx 0$ result in "dueling" rifts, cases with $U_{rate} - U_{mig} \leq \sim -2$ km Myr^{-1} do not jump, and for $U_{rate} - U_{mig}$ increasing from ~10 to ~20 km Myr^{-1} cases result in repeat ridge jumps and finally no jumps.

[35] The tendency for plume influence to increase with $q_{\max}/(Q_{cool}/Z_{lith})$ is mostly intuitive, whereas the changes in behavior with $U_{rate} - U_{mig}$ is less straightforward but reflects different ways in which ridge jumps are influenced by melt transport and magmatic heating. For example, increases in U_{rate} promote ridge jumps by decreasing lithospheric thickness and slope $\partial Z_{lith}/\partial X$ at a given distance ΔX (i.e., less melt is transported to the ridge). Increases in the absolute value of $U_{rate} - U_{mig}$ inhibit ridge jumps by increasing the rate that the plate moves through the hot spot heating zone, thus decreasing the time a given piece of lithosphere can be heated. The direction or sign of $U_{rate} - U_{mig}$ is also important. When $U_{rate} - U_{mig} < 0$ (absolute plate motion to the left in Figure 6) older, thicker lithosphere that has seen less magmatic heating is being delivered to the magmatic heating zone, but when $U_{rate} - U_{mig} > 0$ (absolute plate motion to the right in Figure 6) younger, thinner lithosphere that has seen extensive magmatic heating is being delivered to the magmatic heating zone. The above effects sometimes compete and sometimes reinforce each other to varying degrees.

3.5. Variations in Plume Temperature and Buoyancy Flux

[36] Figure 7 displays how t_{jump} is influenced by changes in plume excess temperature ΔT_p and the width of the plume (the effects of changing width with constant ΔT_p are shown in terms of the resulting changes in buoyancy flux B for ease of comparison to other work). We vary ΔT_p and B for two different types of cases. For type 1, the values of both β and w_{lith} are artificially held constant ($\beta w_{lith} = 1.5 \times 10^{-13}$ s^{-1}) across a zone of heating 12 km wide, the half spreading rate is 10 km Myr^{-1}, and the fixed plume-ridge separation distance is 100 km. For type 2, magmatic heating is calculated from (11)–(15a) and (15b), $\beta = 6.5 \times 10^{-5}$ m^{-1}, $q_{\max} = 0.91 \times 10^{-6}$ J m^{-3} s^{-1}, the off-axis magmatic heating zone varies in width through time between 15 and 100 km, half spreading rate is 20 km Myr^{-1}, and plume-ridge separation distance is 200 km.

[37] For cases of type 1, changes in ΔT_p and B only influence heat conduction and stress in the mantle but do not change the (fixed) magmatic heating rate in the lithosphere. The value of t_{jump} increases with increasing ΔT_p (Figure 7a) but decreases with increasing B at fixed ΔT_p (Figure 7b). Although larger ΔT_p result in larger B, the principle control on t_{jump} when ΔT_p is increased is weakening of the ridge axis caused by the warmer underlying mantle. When B is increased without changes in ΔT_p (larger volume flux), the decrease in t_{jump} is promoted by an increase in lithospheric

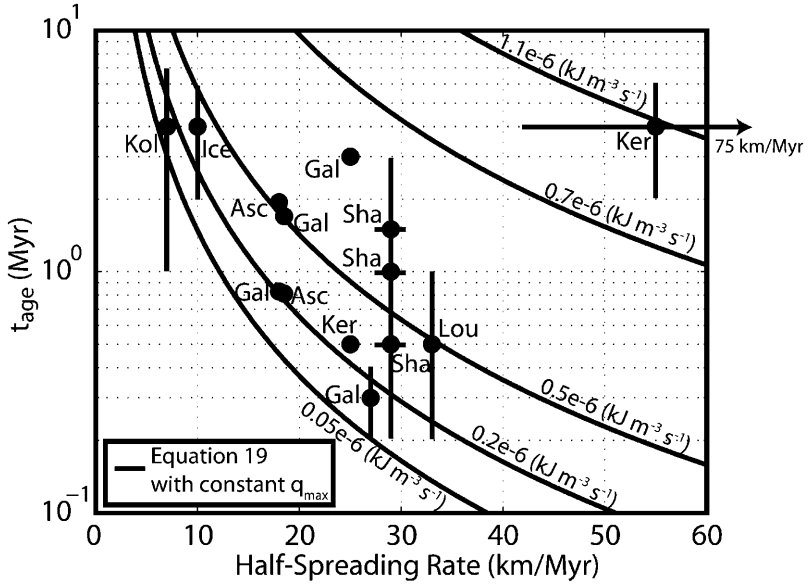

Figure 8. Observed half spreading rates and age of the lithosphere where jumps occurred t_{age} are shown (black circles) for several locations including the Ascension hot spot (Asc), the Galapagos hot spot (Gal), Iceland (Ice), the Kerguelen hot spot (Ker), the Kolbeinsey Ridge (Kol), the Louisville hot spot (Lou), and Shatsky Rise (Sha). Bars show the estimated observation error. When no error bars are present, errors are either smaller than the symbol or unknown. Curves for different maximum heating rates $q_{\max}$ (units are in kJ m^{-3} s^{-1}) are from equations (20a) and (20b). Ridge jumps are predicted to occur below any one curve for a given $q_{\max}$. Data are from *Breivik et al.* [2006], *Brozena and White* [1990], *Desa et al.* [2006], *Géli et al.* [1998], *Hardarson et al.* [1997], *Krishna et al.* [1995], *Krishna and Rao* [2000], *LaFemina et al.* [2005], *Mjelde et al.* [2008], *Nakanishi et al.* [1999], *Sæmundsson* [1974], *Small* [1995], and *Wilson and Hey* [1995].

tension above the plume due to the enhanced shear between the spreading plume material and the overlying plate.

[38] For cases of type 2, changes in ΔT_p and B cause changes not only in mantle temperature and the stress field, but they also change the melt supply from the plume. Unlike the cases of type 1, increases in ΔT_p and B for type 2 both lead to decreases in t_{jump} (Figures 7a and 7b). Over the range of ΔT_p examined (300°C–350°C), there is a large decrease in t_{jump} (~3 Myr) due to increasing values of magma flow rate through the lithosphere associated with greater plume melting. In fact, for the case shown in Figure 7, values of $\Delta T_p \leq 250$°C do not result in a ridge jump. Like type 1, type 2 cases predict a decrease in t_{jump} with larger values of B, but the sensitivity to B is larger, presumably because of the added dependence of melt generation on B.

4. Discussion

4.1. Mid-ocean Ridge Jumps: Predicted Trends and Observations

[39] Mid-ocean ridge jumps associated with plume-ridge interaction are observed near current and former locations of many hot spots including Iceland [*Hardarson et al.*, 1997; *Jóhannesson*, 1980], the Galapagos [*Wilson and Hey*, 1995], Ascension [*Brozena and White*, 1990], Shona [*Small*, 1995], Shatsky Rise [*Nakanishi et al.*, 1999], Louisville [*Géli et al.*, 1998; *Small*, 1995], and along the Ninety-East Ridge [*Desa et al.*, 2006; *Krishna et al.*, 1995; *Krishna and Rao*, 2000; *Small*, 1995]. In Figure 5c, we compare the trend predicted by equations (20a) and (20b) to observed values of t_{jump}/t_{age} and ΔX and inferred values of $q_{\max}$ at four hot spots: Ascension, Iceland (since ~16 Ma), Galapagos (at 10 Ma), and Louisville. Again the inferred values of $q_{\max}$ come from equation (19) and observationally constrained values of Q_{cool} (Figure 5b). The observed values of t_{jump} are constrained by magnetic and bathymetric observations at Ascension (~0.7 Myr [*Brozena and White*, 1990]), dating of rift zone lavas at Iceland (~8 Myr [*Hardarson et al.*, 1997]), models of magnetic anomalies at the Galapagos requiring 3–4 jumps between 5 and 10 Ma (~1.6–2.5 Myr [*Wilson and Hey*, 1995]), and the width of magnetic anomaly 2A at Louisville (~≤1 Ma [*Small*, 1995]). The values of t_{age} are from references in Figure 6 or calculated as described in Table 2. In Figure 5c, Iceland, the Galapagos, and Louisville plot very close to the predicted trend suggesting that the value of $q_{\max}$ for these hot spots may be close to the actual value. However, the predicted value of the minimum $q_{\max}$ to jump for the Ascension hot spot is much smaller than that suggested by equation (20a), implying that the actual $q_{\max}$ is larger than we have inferred. The hot spots show general agreement with the trend predicted by equation (20b), suggesting that our models capture the major processes involved in ridge jumps (i.e., lithospheric weakening) and that other processes including postrift ridge propagation are short relative to t_{jump}.

[40] Figure 8 shows the relationship between observed values of U_{rate} at the time of a ridge jump and t_{age} for 14 documented ridge jumps. Also shown are a set of theoretical curves based on the model results (equation (19)) of the

maximum t_{age} and U_{rate} to initiate a ridge jump (jumps are predicted to occur below, not above, the curves) at a given value of q_{max}. Observed values of U_{rate} and t_{age} are from the references in Figure 8 or are estimated using published magnetic anomalies with error bars based on anomaly width. For the special case of the jump from the extinct Aegir Ridge toward the Iceland hot spot into continental lithosphere to form the Kolbeinsey ridge (Kol, Figure 8), the value of t_{age} is taken as the equivalent age of oceanic lithosphere with the same depth-integrated yield strength. This yield strength was calculated with the thermal, lithological, and rheological parameters of *Mjelde et al.* [2008] at 45 Ma with an estimated lithosphere-asthenosphere boundary depth of 30–40 km. Large error bars in Figure 8 reflect the uncertainty of the assumptions used here for Kolbeinsey. The theoretical curves predict ridge jumps to be restricted to younger plate ages for larger values of spreading rate (for a given value of q_{max}). At a given spreading rate, the theoretical minimum value of q_{max} is smaller for jumps to younger seafloor. The curves illustrate the model predictions that ridge jumps are favored at younger seafloor and jumps to older seafloor require large magma fluxes or slow spreading rates.

[41] Indeed, although the data likely represent a range of poorly constrained values of q_{max} and specific tectonic environments in detail, the above locations show a general decrease in the observed t_{age} for larger values of spreading rate, which is consistent with the trends of the theoretical curves. The favorability of jumps to young seafloor is also reflected by 11 of the 14 jumps occurring in seafloor ≤3 Myr old. Of jumps that occur to seafloor older than 3 Myr, the most recent jump at Iceland and the jump from the extinct Aegir ridge to the Kolbeinsey ridge ("Ice" and "Kol," Figure 8) both occurred in very slowly moving lithosphere (half spreading rates ≤10 km Myr^{-1}). The remaining large jump along the Ninety-East Ridge into ~8 Myr old seafloor [*Krishna and Rao*, 2000] appears to require an unusually large magmatic heating rate compared to other cases.

4.2. Repeat Ridge Jumps

[42] At many locations including Iceland since ~16 Ma [*Hardarson et al.*, 1997; *Jóhannesson*, 1980], Shatsky Rise [*Nakanishi et al.*, 1999], and along the Ninety-East Ridge [*Desa et al.*, 2006; *Krishna et al.*, 1995; *Krishna and Rao*, 2000], proximal ridge segments often jump repeatedly toward the hot spot as the rest of the plate boundary migrates away from the hot spot. Alternatively, the hot spot might capture a ridge segment through asymmetric spreading, such as at the Galapagos between ~5 and ~2.5 Ma during which the ridge remained fixed with the hot spot without resolvable discrete ridge jumps [*Hey*, 1977; *Wilson and Hey*, 1995]. Finally, the hot spot and ridge can separate without a jump as has occurred at the Galapagos since ~2.5 Ma [*Wilson and Hey*, 1995]. While such observations are widely documented, the mechanisms controlling ridge jumps are not.

[43] Our models predict that it is the dynamic evolution of magma flux through and corresponding heating of the lithosphere that is the primary process leading to repeat jumps. Without magma transport calculations, the models of *Mittelstaedt et al.* [2008] predicted a jump to capture the ridge and cause it to migrate steadily with the heating zone, without any repeat ridge jumps. With magma transport calculations, however, repeat ridge jumps are predicted. The key is the separation of the plume away from the ridge axis and the development of a new off-axis peak in magma flux after the previously sloping solidus, shoals and flattens above the plume. Thus, with a more-or-less steady rate of melt production by the plume and a steadily migrating ridge, our models predict an ever changing melt transport system with punctuated changes in ridge geometry.

[44] In Figure 6, model predictions of the inferred minimum q_{max} to jump (Figure 5b) and observationally constrained values of Q_{cool}/Z_{lith} and $U_{rate} - U_{mig}$ are used to plot a set of natural hot spot–ridge systems where repeat ridge jumps are observed: Ascension, Iceland, and the Galapagos. The value of $U_{rate} - U_{mig}$ for each system is determined from the references in the caption of Figure 6. A variation of ±10% of the published spreading rates is imposed (Table 2). The estimates of U_{mig} and U_{rate} for Ascension are modern values [*Brozena and White*, 1990], those from Iceland are from 11 Ma [*Jones*, 2003] and three values of U_{rate} are used for the Galapagos, one at 10 Ma, a second at 4 Ma, and the third from the present (i.e., 0 Ma) [*Wilson and Hey*, 1995]. The three values used for the Galapagos correspond to observed repeat jumps (10 Ma), ridge capture (4 Ma), and no jumps (since ~2.5 Ma) [*Wilson and Hey*, 1995]. The values of $q_{max}/(Q_{cool}/Z_{lith})$ predicted for Ascension, Iceland, and the Galapagos (at 10 Ma) all fall within the range of repeat jumps, in agreement with observations.

[45] For the Galapagos at 4 Ma when the ridge was apparently captured, the inferred value of $q_{max}/(Q_{cool}/Z_{lith})$ is smaller than predicted for this behavior. This result is consistent with the actual q_{max} being larger than we have inferred from equation (19) (up arrow in Figure 6a), which again describes the minimum value required for a jump. At present-day Galapagos (Gal0), which we consider to be without a ridge jump, the inferred $q_{max}/(Q_{cool}/Z_{lith})$ appears to be larger than predicted for no jumps. This result implies the actual q_{max} being less than that inferred (down arrow Figure 6a). Thus, the changing behavior at the Galapagos hot spot implies an increase in magmatic heating between ~10 Ma and ~5 Ma (shift from repeat jumps to ridge capture) and a decrease in magmatic heating at ~2.5 Ma (shift from ridge capture to no jumps). This evolution is similar to changes in estimated magma volume flux at the Galapagos Islands over the past ~8 Myr (Figure 6b) [*Ito et al.*, 1997].

4.3. Ridge Jumps and the Location of Ridges Relative to Hot Spots

[46] A recent study by *Jellinek et al.* [2003] noted that hot spots not associated with the Pacific and African superplumes are commonly clustered within ~1000 km of slow spreading, but not fast spreading ridges. They suggested that off-axis hot spot formation is inhibited by plume material being drawn into the corner flow at fast spreading ridges but not at slow spreading ridges. Another possible reason for hot spots to be located near slow spreading ridges is the capture of a ridge by a mantle plume through repeat ridge jumps and asymmetric spreading. Ridge jumps are predicted to be promoted by slow spreading rates (equation (20a) and Figures 5c and 8). In addition, as a ridge and plume separate, under certain model conditions, the ridge is predicted to remain near the plume for long periods of time. Over time, repeat ridge jumps result in asymmetric accretion as observed near many hot spots [*Müller et al.*, 1998, 2001]

and could well explain the distribution of hot spots and ridges today.

4.4. Intraplate Hot Spots: Contribution of Magmatic Heating to Plate Thinning

[47] Magmatic heating in the model predicts appreciable amounts of lithospheric thinning above a plume, ranging from maximal thinning to cause a ridge jump, to broad regions of more subdued thinning. Such thinning is likely to contribute, at least locally, to elevating the hot spot swell. These predictions are consistent with recent seismic observations that suggest the lithosphere beneath the Hawaiian islands thins from ~100–110 km beneath the island of Hawaii (normal 90 Myr old plate thicknesses) to ~50–60 km beneath Oahu and Kauai, ~500 km downstream [*Li et al.*, 2004]. Previously suggested mechanisms for plume-induced thinning of the Hawaiian lithosphere include conductive heating of the plate by the warm plume material, small-scale convection, and solid-state lithospheric erosion [*Detrick and Crough*, 1978; *Li et al.*, 2004; *Moore et al.*, 1998; *Ribe and Christensen*, 1994]. Heating of a plate by magma as it penetrates the lithosphere provides another mechanism for lithospheric thinning above the Hawaiian plume and at other intraplate hot spots.

5. Conclusions

[48] We explore the combined effects of plume-lithosphere interaction and magmatic heating of the lithosphere on the initiation of ridge jumps. We use a 2-D model of viscoplastic mantle flow with a strain-history-dependent yield criteria coupled to a model of melting and melt transport, which is used to compute heating of the lithosphere where magma passes through it. The melt transport equations simulate the average flow of melt in a channel of high porosity at the solidus, just beneath the lithosphere. The ability of magma to reach the seafloor depends on a balance between the melt pressure at the solidus, the strength of the lithosphere, and the accumulated magmatic damage of the lithosphere. Calculations predict a dynamic focusing of magma penetrating and heating the lithosphere over widths (~10–20 km) comparable to the width of the neovolcanic zone at many mid-ocean ridges [e.g., *Karsten et al.*, 1986] and the widths of hot spot islands. This focusing of magmatism is critical for ridge jumps to occur and is predicted to be caused by a positive feedback between local shoaling of the solidus associated with lithospheric thinning, increased flow of melt toward the locally shallow solidus, and accumulation of magmatic damage.

[49] Model results show that the time to a ridge jump decreases for larger values of the magmatic heating rate and spreading rate, and smaller values of plate age. The inverse relationship with spreading rate is due to increased melt transport velocities up a steeper solidus slope; ridgeward melt transport is faster beneath slower spreading lithosphere because of its larger slope, leading to a greater on-axis but smaller off-axis heating rate (i.e., larger t_{jump}). A hot, plume-like upwelling introduces competing effects. Although larger plume excess temperatures inhibit ridge jumps by weakening the ridge axis, the dominant effect is to promote jumps by increasing melt supply off axis. Ridge jumps are also promoted by increases in the volume flux of the plume due to both increases in melt flux and larger shear stresses on the base of the plate.

[50] Models predict five main behaviors, including repeat ridge jumps, when ridges migrate relative to plumes due to the dynamic interaction between melt transport, lithospheric magma penetration, and the shape of the base of the lithosphere. As the influence of the plume on the ridge axis increases, the models predict: no jumps, dueling rifts, single jumps, repeat ridge jumps and total ridge capture. Plume influence increases with increasing $q_{\max}/(Q_{cool}/Z_{lith})$, the ratio of the maximum magmatic heating rate to the thermal resilience per thickness of lithosphere. A maximum in plume influence is found for slightly positive values of $U_{rate} - U_{mig}$. From this maximum, plume influence generally decreases more rapidly as $U_{rate} - U_{mig}$ becomes increasingly negative and more slowly as $U_{rate} - U_{mig}$ becomes increasingly positive.

[51] Model predictions show favorable agreement with observations at natural plume-ridge systems. Observations at Ascension, Iceland, Louisville and the Galapagos support predicted trends in the timescale of jumps as a function of seafloor age to where jumps occur. Our models predict variations in the Galapagos hot spot heating rate over the past ~10 Myr, similar to independent estimates of changes in magma volume flux at the Galapagos Islands. In addition, observations at 14 ridge jumps support the prediction that ridge jumps are promoted on slower, younger seafloor. Model results also suggest that magmatic heating of the lithosphere is a potential mechanism for lithospheric thinning above intraplate hot spots such as Hawaii. Finally, the process of repeat ridge jumps and ridge capture might explain the observed clustering of hot spots near the slow spreading Mid-Atlantic Ridge.

Appendix A

A1. Melt Transport Equations

A1.1. Equations of Two-Phase Flow

[52] The following equations describe the conservation of mass and momentum of a buoyant, low-viscosity fluid interacting with a deformable, porous, high-viscosity (i.e., solid) matrix [*McKenzie*, 1984]

$$\frac{\partial \rho_m \phi}{\partial t} + \nabla \cdot (\rho_m \phi \mathbf{u}_m) = \Gamma, \tag{A1}$$

$$\frac{\partial \rho_s (1-\phi)}{\partial t} + \nabla \cdot (\rho_s (1-\phi)\mathbf{U}) = -\Gamma, \tag{A2}$$

$$\phi(\mathbf{u_m} - \mathbf{U}) = -\frac{\mathbf{k}}{\mu_m}[\nabla(P - \rho_m g z)], \tag{A3}$$

$$\nabla P = \nabla \cdot \left(\eta\left[\nabla \mathbf{U} + \nabla \mathbf{U}^T\right]\right) + \nabla\left[\left(\varsigma - \frac{2}{3}\eta\right)\nabla \cdot \mathbf{U}\right] + \overline{\rho} g, \tag{A4}$$

where ρ_m and ρ_s are the melt and the solid densities respectively, $\mathbf{u_m}$ is the melt velocity (bold symbols denote vector quantities), $\mathbf{U}$ is the matrix velocity, g is the acceleration of gravity, $\mathbf{k}$ is the permeability tensor, ϕ is the porosity of the solid, t is time, μ_m is the viscosity of the melt, P is the fluid pressure, η and ς are the shear and "effective" bulk viscosities of the solid, and $\overline{\rho} = \rho_m \phi + \rho_s(1-\phi)$ is the average density of the system. The first two equations describe the conservation of mass of the melt and the solid,

respectively, with the transfer of mass between the two phases being governed by the melting rate Γ. Equation (A3) is a modified version of Darcy's law, describing momentum conservation of the melt phase, and (A4) describes conservation of momentum of the solid matrix.

A1.2. Simplified Equations for Transport in the Mantle and a High-Porosity Channel Beneath the Lithosphere

[53] The location and magnitude of magma flow rate through the lithosphere (i.e., out of the mantle) is calculated by using a set of simplified equations of melt flow through, along, and across the top of the melting zone (i.e., the solidus). The simplification that pressure gradients associated with matrix shear and compaction are negligible compared to that associated with melt buoyancy (i.e., the zero compaction length approximation), allows the two momentum equations (A3) and (A4) to be solved separately and is a reasonable approximation for mantle viscosities $\leq\sim 10^{19}$ Pa s [*Spiegelman*, 1993]. Thus in the low-viscosity melting zone, melt rises vertically, and at the very top of the melting zone migrates in a high-porosity channel parallel to the impermeable freezing boundary at the solidus, just below the lithosphere [*Sparks and Parmentier*, 1994; *Spiegelman*, 1993].

[54] Melt flow in the sublithospheric channel is described using a Cartesian coordinate system in which x is parallel to and z is perpendicular to the average slope of the solidus. The simplified forms of (A1) and (A3) in this channel are thus

$$\frac{\partial \rho_m \phi}{\partial t} + \rho_m \left(\frac{\partial u}{\partial x} + \frac{\partial w}{\partial z} \right) = 0 \tag{A5}$$

$$u = \frac{-k_0 \phi^n}{\mu_m} (\rho_s - \rho_m) g \left[\sin(\theta) + \Delta Z \frac{\partial \phi}{\partial x} \right], \tag{A6}$$

where ϕ is the local average porosity in the channel, k_0 is the reference permeability, θ is the local angle of the solidus relative to the horizontal (perpendicular to the pull of gravity), ΔZ is the thickness of the channel, and u and w are the average melt flow rates (or flux per cross-sectional area) in the direction parallel and perpendicular to the solidus x. Partial derivatives describing small changes in the directions of x and z with respect to an absolute, orthonormal reference frame are neglected. In (A6), the forces driving solidus-parallel flow are melt buoyancy and the pressure gradient associated with lateral (i.e., parallel to x) variations in ϕ. The last term of (A6) accounts for gradients in ϕ causing lateral diffusion of porosity and is based on the assumption that the solidus-parallel pressure gradient is the derivative of the overburden at the solidus depth $Z_{solidus}$ plus the mean melt buoyancy in the high-porosity layer, where pressure is

$$P = \rho_s g Z_{solidus} + (\rho_s - \rho_m) \phi(x) g \frac{\Delta Z}{2}. \tag{A7}$$

[55] The flow rate (per area) of melt into the channel, w_{mantle}, is proportional to total rate of melt produced below each point of the channel

$$w_{mantle} = -\int_{Z_{\max}}^{Z_{solidus}} \left(\frac{dF}{dP} \right) \rho_s g \mathbf{W} dZ. \tag{A8}$$

The rate that melt rises across the solidus out of the channel is described as Darcy flow through the overlying lithosphere

$$w_{lith} = \frac{-k_0 \Phi^n}{\mu_m} (\rho_s - \rho_m) g \cos(\theta), \tag{A9}$$

where Φ is the depth-averaged porosity in the lithosphere. The gradient $\partial w/\partial z$ across the channel is approximated as $(w_{lith} - w_{mantle})/\delta$, where δ is the porosity diffusion length scale. Combining (A5)–(A9) yields a single 1-D equation describing the transport of porosity along the solidus,

$$\frac{\partial \phi}{\partial t} - \frac{\Delta \rho g k_0}{\mu_m} \frac{\partial}{\partial x} \left(\phi^n \sin(\theta) + \Delta Z \phi^n \frac{\partial \phi}{\partial x} \right) = \frac{w_{mantle} - w_{lith}}{\delta}. \tag{A10}$$

[56] To isolate the fundamental parameters that govern porosity in the channel, we define the following dimensionless quantities (denoted with primes) according to

$$x = \delta x', \tag{A11a}$$

$$t = \tau\, t', \tag{A11b}$$

$$\phi = \phi_0 \phi'^n, \tag{A11c}$$

$$k = k_0 \phi'^n, \tag{A11d}$$

$$w_{mantle} = w_{m0} w'_{mantle}, \tag{A11e}$$

$$w_{lith} = w_{l0} w'_{lith}, \tag{A11f}$$

$$u = u_0 \phi'^n. \tag{A11g}$$

The characteristic dimensional scales are

$$\tau = \frac{\delta^2}{\kappa_0}, \tag{A11h}$$

$$\kappa_0 = \Delta Z \frac{\Delta \rho g}{\mu_m} k_0 \phi_0^n, \tag{A11i}$$

$$w_{m0} = \frac{\delta \phi_0}{\tau}, \tag{A11j}$$

$$u_0 = \frac{\Delta \rho g}{\mu_m} k_0 n \phi_0^{n-1}, \tag{A11k}$$

$$w_{l0} = \frac{\Delta \rho g}{\mu_m} k_0 \left(\frac{\Phi_{\max}}{2} \right)^n, \tag{A11l}$$

where ϕ_0 is the reference porosity (see Table 1 for parameter definitions). The dimensionless form of (A10) is then

$$\frac{\partial \phi'}{\partial t'} - \frac{\partial}{\partial x'} \left[\phi'^n \frac{\partial \phi'}{\partial x'} \right] - Pe \left[\phi'^{n-1} \sin(\theta) \frac{\partial \phi'}{\partial x'} - \frac{\phi'^n}{n} \cos(\theta) \frac{\partial \theta}{\partial x'} \right] = w'_{mantle} - \frac{w_{l0}}{w_{m0}} w'_{lith}. \tag{A12}$$

Only two parameters therefore control the transport of melt along the base of the solidus: (1) the characteristic ratio of melt flow rate into the lithosphere relative to that from below w_{l0}/w_{m0} and (2) Pe (= $u_0\delta/\kappa_0$, Peclét number), which describes the relative strength of advective upslope flow of melt along the base of a sloping solidus.

A1.3. Function Controlling Lithosphere Penetration Rate of Magma, w_{lith}

[57] To complete the description of melt transport, we must define a function for lithosphere penetration rate w_{lith}, which depends on the depth-averaged lithospheric porosity Φ according to (A9). Following *Hieronymus and Bercovici* [2001], we assume that an incremental change in Φ is controlled by incremental changes in the excess melt pressure at the base of the lithosphere σ_p and damage ε (generally due to chemical, physical, and thermal processes) of the lithosphere caused by magma passing through it:

$$Cd\Phi = d\sigma_p + L_0 d\varepsilon, \tag{A13}$$

where L_0 is a constant and C is defined such that the porosities in the lithosphere vary between 0 and the maximum allowable porosity, $\Phi_{\max}$,

$$C = \frac{C_0}{\Phi(\Phi_{\max} - \Phi)}. \tag{A14}$$

Substituting (A14) into (A13) and integrating yields an equation for lithospheric porosity,

$$\Phi = \frac{\Phi_{\max}}{2}\left[1 + \tanh\left(\frac{A_0\phi\cos(\theta) - \sigma_c + L_0 H}{2C_0/\Phi_{\max}}\right)\right]. \tag{A15}$$

Thus, Φ is controlled by the balance between the melt driving pressure from the high-porosity channel $\sigma_p = A_0\phi\cos(\theta)$, the intrinsic (constant) strength of the lithosphere σ_c, and the damage associated with erosion of the lithosphere as magma passes through it L_0H, where H is a fraction of the time-integrated melt flux (see below). Lithosphere porosity Φ increases in response to a combination of increasing melt pressures and time-integrated magmatic damage (~H).

[58] The value of H evolves according to the following dimensional advection equation:

$$\frac{\partial H}{\partial t} = w_{lith} - \frac{\partial(HU_{rate})}{\partial X} - \frac{S}{(H + H_0)^2}, \tag{A16}$$

where U_{rate} is the speed of the overlying lithosphere and X is horizontal distance in the absolute reference frame (i.e., not along the solidus). The second term on the right-hand side describes advection due to plate motion and the last term describes healing of damage. Without the last two terms, H would equal $\int w_{lith}dt$, the total thickness of magma that penetrated a given section of lithosphere. The healing rate (last term) is assumed to be proportional to the conductive cooling rate; the pertinent width scale ΔX for temperature variations in the zone of magma penetration is proportional to how much magma has passed through it H. Consequently,

$$\text{healing rate} \propto -\frac{\partial T}{\partial t} \propto \frac{\partial^2 T}{\partial X^2} \propto \Delta X^{-2} \propto H^{-2} \tag{A17a}$$

and therefore

$$\text{healing rate} \equiv \frac{S}{(H + H_0)^2}, \tag{A17b}$$

where S and H_0 are constants. Equation (A17) yields greater healing rates for smaller integrated magma fluxes and a maximum healing rate of S/H_0^2,which is effectively the minimum magma penetration rate needed to create new damage (i.e., $w_{lith} - S/H_0^2 > 0$ in (A16)) and thus increase porosity (equation (A15)).

[59] The porosity equation (A15) is expressed terms of dimensionless parameters using H_0 and the (sublithospheric) pressure scale $A_0\varphi_0$:

$$\Phi = \frac{\Phi_{\max}}{2}\left[1 + \tanh\left(\frac{\phi'\cos\theta - \sigma_c' + L_0' H'}{D'}\right)\right], \tag{A18}$$

where $\sigma_c' = \sigma_c/(A_0\phi_0)$, $L_0' = H_0L_0/(A_0\phi_0)$, $H' = H/H_0$, and $D' = 2C_0/(\Phi_{\max}A_0\phi_0)$. The corresponding dimensionless form of the equation for lithospheric melt penetration rate (A9) is

$$w_{lith}' = \frac{w_{lith}}{w_{l0}} = \cos\theta\left[1 + \tanh\left(\frac{\phi'\cos\theta}{D'} - \frac{\sigma_c'}{D'} + \frac{L_0' H'}{D'}\right)\right]^n. \tag{A19}$$

Equation (A19) states that the melt penetration rate is controlled by the balance between the scaled porosity ϕ' in the sublithospheric channel, the scaled strength of the lithosphere σ_c', and the effect of magmatic damage $L_0'H'$. Penetration rate w_{lith}' varies from 0 to its maximum value of $4\cos(\theta)$ (for $n = 2$).

[60] In summary, the three equations governing melt transport are (A12), (A16) and (A19). Transport in the sublithospheric channel (A12) is controlled by two input parameters: w_{l0}/w_{m0} and Pe; the other two equations describing lithosphere penetration by magma require four input parameters: S, D', σ_c', and L_0'. Numerically, the diffusion term in (A12) is treated with centered differencing and the advective terms by upwind differencing. In (A12) and (A16), time is advanced using a first-order, explicit, Euler scheme with a time step ≤50% of the Courant limit.

A2. Benchmarks With Analytical Solutions

[61] To verify the numerical solutions, we compare them to some simple, steady state ($\partial\phi'/\partial t' = 0.0$) analytical solutions which neglect either the terms associated with gradients in porosity (i.e., Pe = large) or the terms accounting for the slope of the solidus (i.e., Pe = 0.0). All cases are shown in Figure A1 with RMS values of the difference between the numerical and analytical solution divided by the maximum porosity of the analytical solutions.

A2.1. Flat Lithosphere, Uniform Melt Flux From Below (Pe = 0.0, w_{lith}' = 0.0, θ = 0.0)

[62] The first case is that of a horizontal solidus that is everywhere impermeable to melt with a uniform melt flux from below. The Peclét number is set to 0 so flow is controlled only by gradients in porosity (A12). Scaled porosity ϕ' is maintained at zero on both the left and right hand sides of the domain (width $L' = 100$). The analytical solution of (A12) is

$$\phi' = \left\{(n+1)\left[\frac{-w_{mantle}' X'^2}{2} + \frac{w_{mantle}' L'}{2}X'\right]\right\}^{1/(n+1)}, \tag{A20}$$

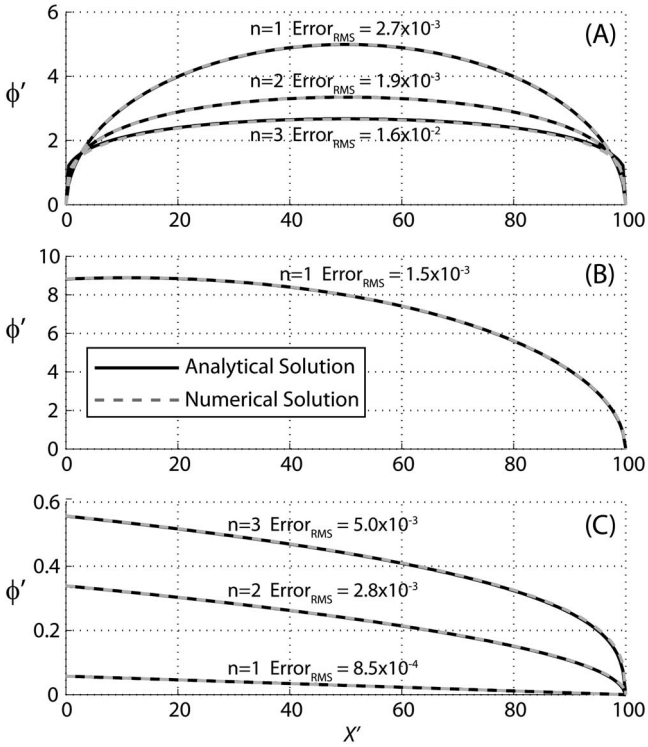

Figure A1. Comparisons of the dimensionless porosities between the analytical solution (dashed lines) and the numerical solution (solid lines; numerical grid spacing 0.5) for steady state melt flow associated with gradients in porosity beneath (a) a flat solidus and with the dimensionless porosity ϕ' fixed at 0.0 on both ends (equation (A20)), (b) a case with a fixed flux on the left-hand side, a flat solidus, and ϕ' fixed at 0.0 on the right-hand side (equation (A21)), and (c) a case dominated by buoyant melt flow up the slope of the solidus with $w'_{mantle}/Pe = 1 \times 10^{-4}$ (equation (A22)). In all cases, the errors shown are the root mean square of the difference between the analytical and numerical solutions divided by the maximum porosity of the analytical solution.

where the uniform melt flux from below w'_{mantle} (= 1.0×10^{-2}) is balanced by the melt flux out the sides of the domain at $x' = 0$ and $x' = 100$. Comparing this solution to the numerical method for $n = 1$, 2, and 3 results in a very close matches with RMS error ≤0.016.

A2.2. Flat Lithosphere With Fixed Melt Sources ($Pe = 0.0$, $\partial\phi'/\partial X' = 0.0125$ at $x' = 0$, $\theta = 0.0$)

[63] The second analytical solution is similar to that in section A2.1, but instead of restricting ϕ' to 0 on the left-hand boundary, a porosity flux of Q' (= $\partial\phi'/\partial X' = 0.0125$) is imposed. The analytical solution for $n = 1$ is

$$\phi' = \left[-w'_{mantle}X'^2 + \left(-Q'^2L' \pm Q'L'\sqrt{Q'^2 + w'_{mantle}}\right)X' + \frac{\left(-Q'^2L' \pm Q'L'\sqrt{Q'^2 + w'_{mantle}}\right)^2}{2Q'^2} \right]^{1/2}. \quad \text{(A21)}$$

This case is somewhat similar to a ridge with melt reaching the seafloor at the axis. The comparison of the two solutions shows an RMS error of 0.0015.

A2.3. Sloped Lithosphere Without Diffusion ($Pe = 100$, $w'_{lith} = 0.0$, $\theta = 10°$)

[64] When Pe is large, the diffusion term in A12 can be neglected and the analytical solution for buoyant melt traveling up a sloping lithosphere is straightforward. Solving the resulting first-order differential equation with the boundary condition of $\phi' = 0.0$ on the right-hand side of the domain yields

$$\phi' = \left[\frac{-nw'_{mantle}}{Pe\sin(\theta)}(X' - L')\right]^{1/n}. \quad \text{(A22)}$$

Comparison with a numerical solution where melt is allowed to flow out of the left boundary and porosity is 0 on the right edge for $n = 1$, 2, and 3 and $w'_{mantle}/Pe = 1 \times 10^{-4}$ results in RMS errors < 0.0050.

[65] **Acknowledgments.** Numerical calculations for this work were performed at the Maui High Performance Computing Center. Mittelstaedt would like to thank the ARCS Foundation for their support of this research with the ARCS Pulley Scholarship in Geology and Geophysics. Mittelstaedt and Ito were funded by OCE03-51234. We thank two anonymous referees and the Associate Editor for their constructive reviews. This is SOEST contribution 7998.

References

Asimow, P. D., M. M. Hirschmann, and E. M. Stolper (1997), An analysis of variations in isentropic melt productivity, *Philos. Trans. R. Soc. London*, *355*, 255–281, doi:10.1098/rsta.1997.0009.

Asimow, P. D., J. E. Dixon, and C. H. Langmuir (2004), A hydrous melting and fractionation model for mid-ocean ridge basalts: Application to the Mid-Atlantic Ridge near the Azores, *Geochem. Geophys. Geosyst.*, *5*, Q01E16, doi:10.1029/2003GC000568.

Bianco, T. A., G. Ito, J. van Hunen, M. D. Ballmer, and J. J. Mahoney (2008), Geochemical variation at the Hawaiian hot spot caused by upper mantle dynamics and melting of a heterogeneous plume, *Geochem. Geophys. Geosyst.*, *9*, Q11003, doi:10.1029/2008GC002111.

Breivik, A. J., R. Mjelde, J. I. Faleide, and Y. Murai (2006), Rates of continental breakup magmatism and seafloor spreading in the Norway Basin - Iceland Plume interaction, *J. Geophys. Res.*, *111*, B07102, doi:10.1029/2005JB004004.

Briais, A., and M. Rabinowicz (2002), Temporal variations of the segmentation of slow to intermediate spreading mid-ocean ridges: 1. Synoptic observations based on satellite altimetry data, *J. Geophys. Res.*, *107*(B5), 2098, doi:10.1029/2001JB000533.

Brozena, J. M., and R. White (1990), Ridge jumps and propagations in the South Atlantic Ocean, *Nature*, *348*, 149–152, doi:10.1038/348149a0.

Canales, J. P., G. Ito, R. Detrick, and J. Sinton (2002), Crustal thickness along the western Galápagos Spreading Center and the compensation of the Galápagos hotspot swell, *Earth Planet. Sci. Lett.*, *203*, 311–327, doi:10.1016/S0012-821X(02)00843-9.

Chen, Y., and W. J. Morgan (1990), A nonlinear rheology model for mid-ocean ridge axis topography, *J. Geophys. Res.*, *95*(B11), 17,583–17,604, doi:10.1029/JB095iB11p17583.

Christensen, U. R. (1984), Convection with pressure- and temperature-dependent non-Newtonian rheology, *Geophys. J. R. Astron. Soc.*, *77*, 343–384.

Davis, R. O., and A. P. S. Selvadurai (2002), *Plasticity and Geomechanics*, 287 pp., Cambridge Univ. Press, New York, doi:10.1017/CBO9780511614958.

Desa, M., M. V. Ramana, and T. Ramprasad (2006), Seafloor spreading magnetic anomalies south of Sri Lanka, *Mar. Geol.*, *229*, 227–240, doi:10.1016/j.margeo.2006.03.006.

Detrick, R., and S. T. Crough (1978), Island subsidence, hot spots, and lithospheric thinning, *J. Geophys. Res.*, *83*, 1236–1244, doi:10.1029/JB083iB03p01236.

Garcia, S., N. Arnaud, J. Angelier, F. Bergerat, and C. Homberg (2003), Rift jump processes in Northern Iceland since 10 Ma from $^{40}Ar/^{39}Ar$ geochronology, *Earth Planet. Sci. Lett.*, *214*, 529–544, doi:10.1016/S0012-821X(03)00400-X.

Géli, L., D. Aslanian, J. Olivet, I. Vlastelic, L. Dosso, H. Guillou, and H. Bougault (1998), Location of the Louisville hotspot and origin of Hollister Ridge: Geophysical constraints, *Earth Planet. Sci. Lett.*, *164*, 31–40, doi:10.1016/S0012-821X(98)00217-9.

Hardarson, B. S., J. G. Fitton, R. M. Ellam, and M. S. Pringle (1997), Rift relocation - a geochemical and geochronological investigation of a paleo-rift in northwest Iceland, *Earth Planet. Sci. Lett.*, *153*, 181–196, doi:10.1016/S0012-821X(97)00145-3.

Harpp, K., and D. Geist (2002), Wolf-Darwin lineament and plume-ridge interaction in northern Galapagos, *Geochem. Geophys. Geosyst.*, *3*(11), 8504, doi:10.1029/2002GC000370.

Hey, R. N. (1977), Tectonic evolution of the Coco-Nazca spreading center, *Geol. Soc. Am. Bull.*, *88*, 1404–1420, doi:10.1130/0016-7606(1977)88<1404:TEOTCS>2.0.CO;2.

Hieronymus, C. F., and D. Bercovici (2001), A theoretical model of hotspot volcanism: Control on volcanic spacing and patterns via magma dynamics and lithospheric stresses, *J. Geophys. Res.*, *106*(B1), 683–702, doi:10.1029/2000JB900355.

Hirth, G., and D. L. Kohlstedt (1995a), Experimental constraints on the dynamics of the partially molten upper mantle: 2. Deformation in the dislocation creep regime, *J. Geophys. Res.*, *100*, 15,441–15,449, doi:10.1029/95JB01292.

Hirth, G., and D. L. Kohlstedt (1995b), Experimental constraints on the dynamics of the partially molten upper mantle: 1. Deformation in the diffusion creep regime, *J. Geophys. Res.*, *100*, 1981–2001, doi:10.1029/94JB02128.

Hirth, G., and D. L. Kohlstedt (1996), Water in the oceanic upper mantle: Implications for rheology, melt extraction, and the evolution of the lithosphere, *Earth Planet. Sci. Lett.*, *144*, 93–108, doi:10.1016/0012-821X(96)00154-9.

Ito, G., J. Lin, and C. W. Gable (1997), Interaction of mantle plumes and migrating mid-ocean ridges: Implications for the Galapagos plume-ridge system, *J. Geophys. Res.*, *102*(B7), 15,403–15,417, doi:10.1029/97JB01049.

Ito, G., J. Lin, and D. Graham (2003), Observational and theoretical studies of the dynamics of mantle plume-mid-ocean ridge interaction, *Rev. Geophys.*, *41*(4), 1017, doi:10.1029/2002RG000117.

Ito, G., and J. Mahoney (2005), Flow and melting of a heterogeneous mantle: 1. Method and importance to the geochemistry of ocean island and mid-ocean ridge basalts, *Earth Planet. Sci. Lett.*, *230*, 29–46, doi:10.1016/j.epsl.2004.10.035.

Jellinek, A. M., H. M. Gonnermann, and M. A. Richards (2003), Plume capture by divergent plate motions: Implications for the distribution of hotspots, geochemistry of mid-ocean ridge basalts, and heat flux at the core-mantle boundary, *Earth Planet. Sci. Lett.*, *205*, 361–378, doi:10.1016/S0012-821X(02)01070-1.

Jóhannesson, H. (1980), Jarðlagaskipan og próun rekbelta á Vesturlandi (Evolution of rift zones in western Iceland), *Náttúrufræðingurinn*, *50*(1), 13–31.

Jones, S. M. (2003), Test of a ridge-plume interaction model using oceanic crustal structure around Iceland, *Earth Planet. Sci. Lett.*, *208*(3–4), 205–218, doi:10.1016/S0012-821X(03)00050-5.

Karato, S., and P. Wu (1993), Rheology of the upper mantle: A synthesis, *Science*, *260*(5109), 771–778, doi:10.1126/science.260.5109.771.

Karsten, J. L., S. R. Hammond, E. E. Davis, and R. G. Currie (1986), Detailed geomorphology and neotectonics of the Endeavour Segment, Juan de Fuca Ridge: New results from Seabeam swath mapping, *Geol. Soc. Am. Bull.*, *97*(2), 213–221, doi:10.1130/0016-7606(1986)97<213:DGANOT>2.0.CO;2.

Katz, R. F., M. Spiegelan, and C. H. Langmuir (2003), A new parameterization of hydrous mantle melting, *Geochem. Geophys. Geosyst.*, *4*(9), 1073, doi:10.1029/2002GC000433.

Kendall, J. M., G. W. Stuart, C. J. Ebinger, I. D. Bastow, and D. Keir (2005), Magma-assisted rifting in Ethiopia, *Nature*, *433*, 146–148, doi:10.1038/nature03161.

Krishna, K. S., and D. G. Rao (2000), Abandoned Paleocene spreading center in the northeastern Indian Ocean: Evidence from magnetic and seismic reflection data, *Mar. Geol.*, *162*, 215–224, doi:10.1016/S0025-3227(99)00085-7.

Krishna, K. S., D. G. Rao, M. V. Ramana, V. Subrahmanyam, K. V. L. N. S. Sarma, A. I. Pilipenko, V. S. Shcherbakov, and I. V. Radhakrishna Murthy (1995), Tectonic model for the evolution of oceanic crust in the northeastern Indian Ocean from the Late Cretaceous to the early Tertiary, *J. Geophys. Res.*, *100*(B10), 20,011–20,024, doi:10.1029/94JB02464.

LaFemina, P. C., T. H. Dixon, R. Malservisi, T. Arnadottir, E. Sturkell, F. Sigmundsson, and P. Einarsson (2005), Geodetic GPS measurements in south Iceland: Strain accumulation and partitioning in a propagating ridge system, *J. Geophys. Res.*, *110*, B11405, doi:10.1029/2005JB003675.

Li, X., R. Kind, X. Yuan, I. Wolbern, and W. Hanka (2004), Rejuvenation of the lithosphere by the Hawaiian plume, *Nature*, *427*, 827–829, doi:10.1038/nature02349.

Mammerickx, J., and D. T. Sandwell (1986), Rifting of old oceanic lithosphere, *J. Geophys. Res.*, *91*, 1975–1988, doi:10.1029/JB091iB02p01975.

McKenzie, D. (1984), The generation and compaction of partially molten rock, *J. Petrol.*, *25*, 713–765.

Mittelstaedt, E., G. Ito, and M. Behn (2008), Mid-ocean ridge jumps associated with hotspot magmatism, *Earth Planet. Sci. Lett.*, *266*(3–4), 256–270, doi:10.1016/j.epsl.2007.10.055.

Mjelde, R., A. J. Breivik, T. Raum, E. Mittelstaedt, G. Ito, and J. I. Faleide (2008), Magmatic and tectonic evolution of the North Atlantic, *J. Geol. Soc.*, *165*, 31–42, doi:10.1144/0016-76492007-018.

Moore, W. B., G. Schubert, and P. Tackley (1998), Three-dimensional simulations of plume-lithosphere interaction at the Hawaiian swell, *Science*, *279*, 1008–1011, doi:10.1126/science.279.5353.1008.

Moresi, L., and V. S. Solomatov (1995), Numerical investigation of 2D convection with extremely large viscosity variations, *Phys. Fluids*, *7*(9), 2154–2162, doi:10.1063/1.868465.

Müller, R. D., J. Royer, and L. A. Lawver (1993), Revised plate motions relative to the hotspots from combined Atlantic and Indian Ocean hotspot tracks, *Geology*, *21*, 275–278, doi:10.1130/0091-7613(1993)021<0275:RPMRTT>2.3.CO;2.

Müller, R. D., W. R. Roest, and J. Royer (1998), Asymmetric sea-floor spreading caused by ridge-plume interactions, *Nature*, *396*, 455–459, doi:10.1038/24850.

Müller, R. D., C. Gaina, W. R. Roest, and D. L. Hansen (2001), A recipe for microcontinent formation, *Geology*, *29*(3), 203–206, doi:10.1130/0091-7613(2001)029<0203:ARFMF>2.0.CO;2.

Müller, R. D., M. Sdrolias, C. Gaina, and W. R. Roest (2008), Age, spreading rates, and spreading asymmetry of the world's ocean crust, *Geochem. Geophys. Geosyst.*, *9*, Q04006, doi:10.1029/2007GC001743.

Nakanishi, M., W. W. Sager, and A. Klaus (1999), Magnetic lineations within Shatsky Rise, northwest Pacific Ocean: Implications for hotspot-triple junction interaction and oceanic plateau formation, *J. Geophys. Res.*, *104*(B4), 7539–7556, doi:10.1029/1999JB900002.

Nielsen, T. K., H. C. Larsen, and J. R. Hopper (2002), Contrasting rifted margin styles south of Greenland: Implications for mantle plume dynamics, *Earth Planet. Sci. Lett.*, *200*, 271–286, doi:10.1016/S0012-821X(02)00616-7.

Parsons, B., and J. G. Sclater (1977), An analysis of the variation of ocean floor bathymetry and heat flow with age, *J. Geophys. Res.*, *82*, 803–827, doi:10.1029/JB082i005p00803.

Poliakov, A. N. B., and W. R. Buck (1998), Mechanics of stretching elastic-plastic-viscous layers: Applications to slow-spreading mid-ocean ridges, in *Faulting and Magmatism at Mid-Ocean Ridges Geophys. Monogr. Ser.*, vol. 106, edited by W. R. Buck et al., pp. 305–323, AGU, Washington, D. C.

Ribe, N. M., and U. R. Christensen (1994), Three-dimensional modelling of plume-lithosphere interaction, *J. Geophys. Res.*, *99*, 669–682, doi:10.1029/93JB02386.

Sæmundsson, K. (1974), Evolution of the axial rifting zone in northern Iceland and the Tjörnes Fracture Zone, *Geol. Soc. Am. Bull.*, *85*, 495–504, doi:10.1130/0016-7606(1974)85<495:EOTARZ>2.0.CO;2.

Sleep, N. (1990), Hotspots and mantle plumes: Some phenomenology, *J. Geophys. Res.*, *95*(B5), 6715–6736, doi:10.1029/JB095iB05p06715.

Small, C. (1995), Observations of ridge-hotspot interactions in the Southern Ocean, *J. Geophys. Res.*, *100*, 17,931–17,946, doi:10.1029/95JB01377.

Sparks, D. W., and E. M. Parmentier (1991), Melt extraction from the mantle beneath spreading centers, *Earth Planet. Sci. Lett.*, *105*, 368–377, doi:10.1016/0012-821X(91)90178-K.

Sparks, D. W., and E. M. Parmentier (1994), The generation and migration of partial melt beneath oceanic spreading centers, in *Magmatic Systems*, edited by M. P. Ryan, pp. 55–76, Academic, San Diego, Calif., doi:10.1016/S0074-6142(09)60092-9.

Spiegelman, M. (1993), Physics of melt extraction: Theory, implications and applications, *Philos. Trans. R. Soc. London*, *342*, 23–41, doi:10.1098/rsta.1993.0002.

Torsvik, T. H., J. Mosar, and E. A. Eide (2001), Cretaceous-Tertiary geodynamics: A North Atlantic exercise, *Geophys. J. Int.*, *146*, 850–866, doi:10.1046/j.0956-540x.2001.01511.x.

van Hunen, J., and S. Zhong (2003), New insight in the Hawaiian plume swell dynamics from scaling laws, *Geophys. Res. Lett.*, *30*(15), 1785, doi:10.1029/2003GL017646.

van Hunen, J., S. Zhong, N. Shapiro, and M. Ritzwoller (2005), New evidence for dislocation creep from 3-D geodynamic modeling of the Pacific upper mantle structure, *Earth Planet. Sci. Lett.*, *238*, 146–155, doi:10.1016/j.epsl.2005.07.006.

Wilson, D. S., and R. N. Hey (1995), History of rift propagation and magnetization intensity for the Cocos-Nazca spreading center, *J. Geophys. Res.*, *100*(B6), 10,041–10,056, doi:10.1029/95JB00762.

Zhong, S., and A. B. Watts (2002), Constraints on the dynamics of mantle plumes from uplift of the Hawaiian Islands, *Earth Planet. Sci. Lett.*, *203*, 105–116, doi:10.1016/S0012-821X(02)00845-2.

Zhong, S., M. T. Zuber, L. Moresi, and M. Gurnis (2000), Role of temperature-dependent viscosity and surface plates in spherical shell models of mantle convection, *J. Geophys. Res.*, *105*(B5), 11,063–11,082, doi:10.1029/2000JB900003.

Zhong, W., and W. Yao (2008), Influence of damage degree on self-healing of concrete, *Construct. Build. Mater.*, *22*, 1137–1142, doi:10.1016/j.conbuildmat.2007.02.006.

G. Ito, SOEST, University of Hawaii, 1680 East West Rd., Honolulu, HI 96822, USA.

E. Mittelstaedt, Laboratoire FAST, CNRS/UPMC/UPS, Batiment 502, rue du Belvedere, F-91405 Orsay CEDEX, France. (mittelstaedt@fast.u-psud.fr)

J. van Hunen, Department of Earth Sciences, Durham University, Durham DH1 3HP, UK.